Wardinski *et al. Earth, Planets and Space* (2026) 78:101
https://doi.org/10.1186/s40623-026-02410-1

Earth, Planets and Space

FULL PAPER **Open Access**

Models and predictions of Earth's magnetic field based on geomagnetic observatory data

I. Wardinski[1*], F. Terra Nova[2,3] and H. Amit[2]

Abstract Observations of the geomagnetic field taken at Earth's surface are processed to construct a set of continuous models of the geomagnetic field and its secular variation from 1956 to 2033. One of these models, the parent model, provides candidate main field models for the epochs 2020 and 2025 to the 14th generation of the International Geomagnetic Reference Field (IGRF). The secular variation candidate model for the period 2025–2030 is derived from a forecast of the secular variation in 2027.5, which results from a multi-variate singular spectrum analysis of the secular variation from 1960 to 2023. Apart from the parent model, we also derive models to higher spherical harmonic degrees than $\ell = 14$ to study small-scale features of the core field and its temporal variation. A comparison with a satellite-based field model indicates a good agreement for the core field, but shows significant differences for the secular variation, which probably could be explained by the different source geometry of the data. Our results suggest a strengthening of the meridional core flow in recent years and the existence of north–south oriented undulations in the radial component of the secular variation which may be related to the presence of waves in Earth's liquid outer core.

Keywords Geomagnetic secular variation, Geomagnetic field models, Forecasts of the geomagnetic field

---

*Correspondence:
I. Wardinski
Ingo.Wardinski@unistra.fr
Full list of author information is available at the end of the article

Graphical Abstract

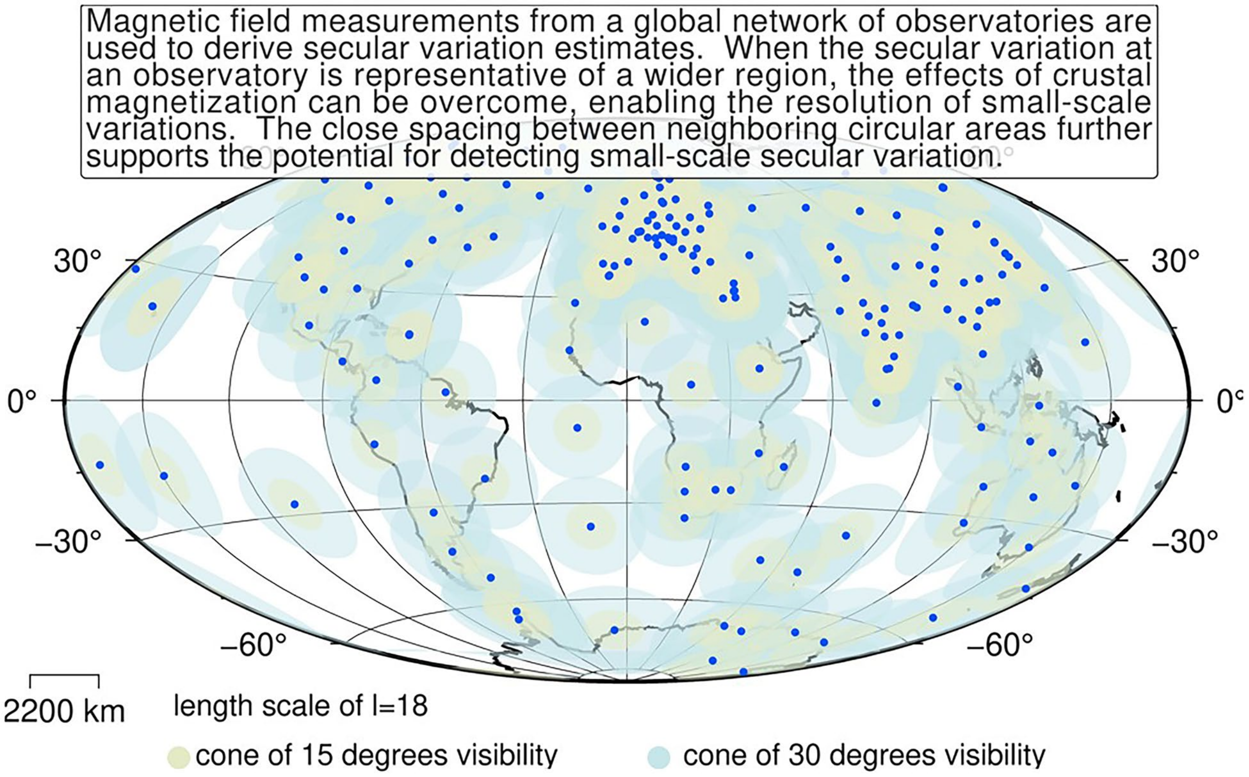

Magnetic field measurements from a global network of observatories are used to derive secular variation estimates. When the secular variation at an observatory is representative of a wider region, the effects of crustal magnetization can be overcome, enabling the resolution of small-scale variations. The close spacing between neighboring circular areas further supports the potential for detecting small-scale secular variation.

1 Introduction

Earth's magnetic field as it is observed originates from various sources within and outside Earth. The largest contribution arises from the action of a dynamo in Earth's liquid outer core. The magnetization of the lithosphere also contributes to the observation as well as different induction processes in the Ocean, ionosphere and the magnetosphere. The last two are considered as external field sources as they lie outside Earth. However, temporal variations of external field sources induce secondary magnetic fields in the lithosphere and the Ocean that appear to be of internal origin from within Earth. The different source mechanisms expose differences in their typical timescales. While the lithospheric field appear to be invariant in time, external, externally induced and core fields vary from seconds to millennia and even longer timescales (Constable and Johnson 2005). In between, on annual and perennial timescales, the temporal variations of these sources overlap. The screening effect of the weakly electrically conducting mantle acts as a filter and sets a limit to the shortest variations of the core field that can pass through. Variations shorter than a year may not pass the mantle (Backus 1983; Benton and Whaler 1983; Holme 1998). Variations on millennial and longer timescales are thought to be affected by the lower mantle thermal heterogeneity (Mound and Davies 2023; de Oliveira et al. 2024; Wardinski et al. 2025).

The wealth of data that have been collected by satellite missions over the past 25 years have led to series of geomagnetic field models (Olsen et al. 2006; Finlay et al. 2016, 2020; Lesur et al. 2008, 2010, 2015) that capture fine details of the geomagnetic field and its temporal variability (Lesur et al. 2022). Recently, such models were derived from satellite data to spherical harmonic degree $\ell > 14$ (Ropp et al. 2020; Finlay et al. 2020) at which the strength of lithospheric contributions dominates the core magnetic field. Here, we compile geomagnetic field observations exclusively taken at Earth's surface to construct a set of continuous models of the geomagnetic core field and its secular variation between 1956 and 2033. Like in the previous versions of our modeling approach (Wardinski and Holme 2006; Wardinski and Lesur 2012; Wardinski et al. 2020) we use secular variation estimates derived from the observatory data to construct these models. One of these models will serve as a parent for our candidate models to the 14th generation of the International Geomagnetic Reference Field (IGRF), which describes Earth's main magnetic field and its secular variation. Previous versions (e.g., Finlay et al. 2010; Thébault et al. 2015; Alken et al. 2021a) are widely used in many disciplines of Earth sciences and applied sciences.

A new aspect of our study is the derivation of core field and secular variation models up to spherical harmonic degree 18 based only on geomagnetic observatory data. In principal this should be possible as the small-scale secular variation is not masked by the magnetization of the lithosphere as it is the case for the magnetic core field and may only be subject to the global distribution of geomagnetic data. We aim to compare our resulting core field and secular variation models to a satellite-based field model CHAOS-7 (version 7.18) (Finlay et al. 2020) and try to identify the source of small-scale field and secular variation features, which may indicate particular dynamical processes in Earth's outer core.

This paper is organized as follows. Section 2 outlines the derivation of secular variation estimates and the modeling technique to derive the parent geomagnetic field model for the IGRF candidates. In the third section, we compare results of our model and the satellite-based CHAOS-7 model. Section 4 provides forecasts of the secular variation for the period 2025 to 2033 based on a multi-variate singular spectrum analysis. The last section discusses the results and concludes the study.

2 Geomagnetic field modeling

In this section, we present the derivation of the secular variation estimates from ground-based geomagnetic observatories and outline our modeling strategies to derive a parent geomagnetic main field model from which we deduce different candidate models for the DGRF 2020, IGRF 2025 and the secular variation forecast for 2027.5.

The parent model, hereafter C^3FM4-P, covers the period from 1956 to 2025. The model derivation follows that of Wardinski and Lesur (2012) and Wardinski et al. (2020) and is a spline-based model of Earth's core field and its secular variation. Like in the previous model, C^3 FM3, we use order 6 B-splines to parameterize field coefficients in time. The spline knot spacing is set to be roughly 1.4 years. The model is constrained to fit a main field model for the epochs 2001 and 2019 which are based on magnetic measurements taken by the CHAMP and Swarm satellite missions (Ropp et al. 2020). We choose 2019 because it is an epoch which provides good data coverage by geomagnetic observatories and the Swarm satellite mission. In general, the data coverage decreases towards the model endpoint.

2.1 Ground-based geomagnetic observatories data

The upper panel of Fig. 1 maps locations of the ground-based geomagnetic observatories used in this study. Measurements taken at this network of geomagnetic observatories are used to derive estimates of secular variation (Wardinski and Holme 2006; Wardinski and Lesur 2012; Lesur et al. 2018). These estimates are obtained by annual differences of observatory monthly means, where these monthly means are averages of observatory hourly means. Also, annual means are used for observatories for which hourly mean values are not available in the World Data Centers (WDC) or Intermagnet data sets (World Data Centre for Geomagnetism - Edinburgh 2019; INTERMAGNET 2020). These observatory annual means are part of a compilation that is provided by the British Geological Survey in Edinburgh (British Geological Survey - Edinburgh 2020). Prior to 1957 the number of observatory monthly means is 51. Over the period 1956–2025 the number of geomagnetic observatories simultaneously in operation that have been providing vectorial hourly means of North, East and downward components ranges between 51 and 155. After mid-2020 the number of annual and monthly means drops below 100. This recent decrease in the number of observatories poses a severe problem for geomagnetic field modeling. In the future the geomagnetic community should set maintenance of geomagnetic surface observatories as a major priority. Most of the times the number of annual means is larger than the number of observatory monthly means; see Fig. 1. In the processing of secular variation estimates, erroneous data were removed when encountered and data gaps were not filled by interpolations. Table 2 in the appendix lists the observatories and the statistical properties of their residuals with respect to the parent model.

2.1.1 Secular variation estimates

We derive secular variation estimates as input for the geomagnetic field modeling. The technique is applied to ground-based geomagnetic monthly means. For example, the secular variation of the X-component at a given observatory is estimated as:

$$dX/dt|_\tau = \big(X(\tau+6) - X(\tau-6)\big)/dt, \tag{1}$$

where τ denotes a particular month. These are annual differences of observatory monthly means. Likewise, observatory annual means are treated using

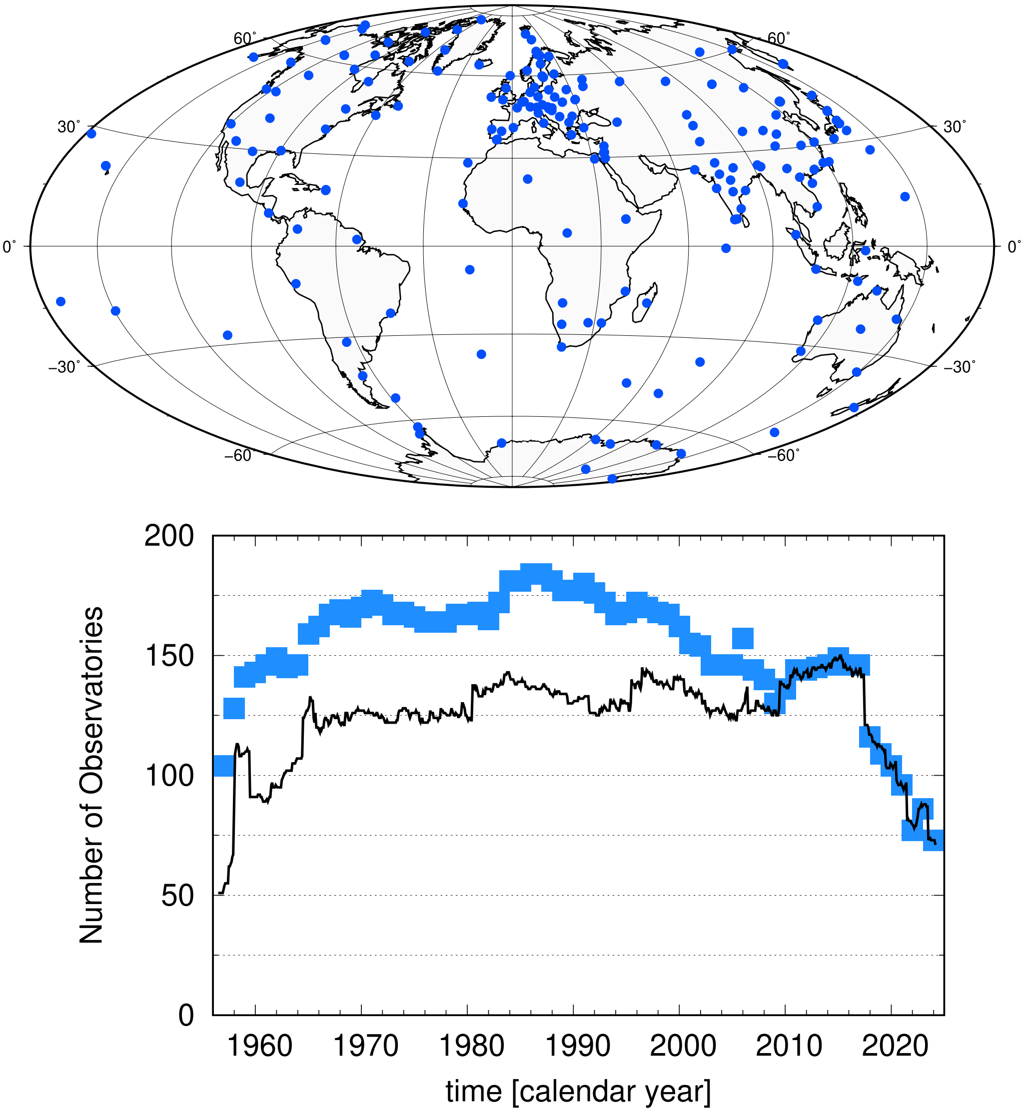

Fig. 1 Locations and the number of available geomagnetic observatories used in this study. The blue squares in the lower panel represent the number of observatory annual means, while the black curve represents the number of observatory monthly means

$$dX/dt|_{t+1/2} = \big(X(t+1) - X(t)\big)/dt, \tag{2}$$

where t is in calendar years and dt is 1 year.

The magnetization of the crust surpasses the strength of the core field at Earth's surface from spherical harmonic degree 15 onward. By applying this approach the magnetic signature of the crust is reduced or eliminated, as it

Table 1 Specifications of the inversion parameters of the parent model and the field model dedicated to study the small-scale secular variation. The quantities that are controlling the model's temporal and spatial smoothness (λ_T, λ_S) are in units nT^{-2}yr^{4}andnT^{-2}, respectively

	λ_T	λ_S	ℓ_{max}	**temp norm [Wb/yr^3]**	**spat norm [Wb]**	**Misfit**
C^{3}FM4-P	3×10^{-2}	7×10^{-7}	14	5.532×10^{6}	59.027×10^{11}	0.5385
C^{3}FM4-Z	3×10^{-2}	7×10^{-7}	18	5.532×10^{6}	59.027×10^{11}	0.5385
C^{3}FM4-S	3×10^{-2}	1×10^{-8}	18	5.408×10^{6}	75.027×10^{11}	0.5354

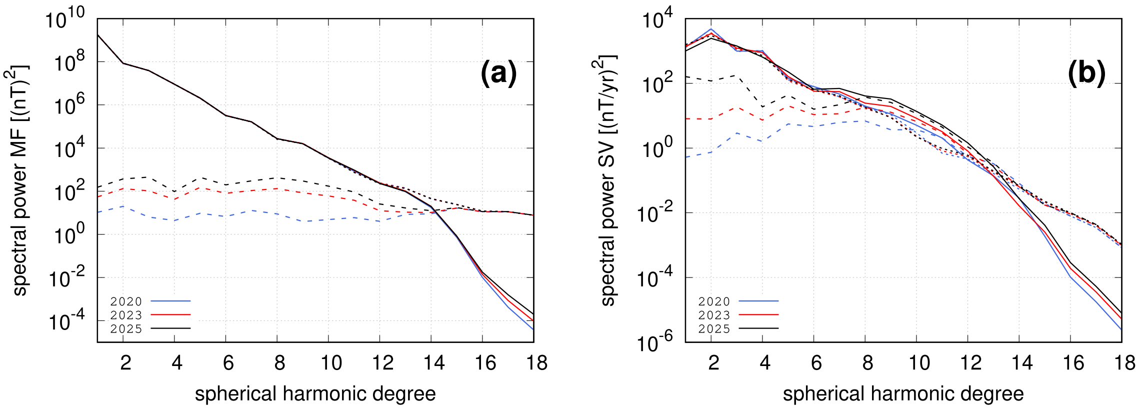

Fig. 2 Spectra of main field models (**a**) and secular variation (**b**) of C^{3}FM4-Z (solid lines) and CHAOS-7 (dotted lines) for different epochs at Earth's surface. Dashed lines represent respective spectra of the differences

can be assumed to be constant with time. This may allow to study small-scale secular variation. A limiting factor is the uneven global distribution of geomagnetic observatories. To this end, the total number of data is 306,774 which correspond to 102,258 vector triplets that are used to characterize the core field and its secular variation.

2.2 Modeling technique

Most geomagnetic field modeling approaches assume Earth's magnetic field $\mathbf{B}(r,\theta,\phi,t)$ to be a potential field without magnetic sources in the mantle and in the vicinity of satellite orbits. Then the geomagnetic field is determined as a gradient of a scalar potential, i.e.,

$$\mathbf{B}(r,\theta,\phi,t) = -\nabla V(r,\theta,\phi,t), \tag{3}$$

where the scalar potential of the geomagnetic field can be represented in a spherical geometry as:

$$\begin{aligned} V(r,\theta,\phi,t) =& a\sum_{l=1}^{\ell_{\max}} \left(\frac{a}{r}\right)^{l+1} \sum_{m=0}^{l} (g_l^m(t)\cos(m\phi) \\ &+ h_l^m(t)\sin(m\phi))P_l^m(\cos\theta). \end{aligned} \tag{4}$$

a is Earth's radius (6371.2 km), (r,θ,ϕ) the geocentric spherical radial, co-latitude and longitude coordinates and $P_l^m(\cos\theta)$ are the Schmidt quasi-normalized associated Legendre functions with degree ℓ and order m. The maximum spherical harmonic degree in (4) is chosen to be $\ell_{\max} = 14$ for the parent model. Two additional models are derived to study small-scale structures of the secular variation. For those, we set $\ell_{\max} = 18$. The Gauss coefficients $\{g_l^m, h_l^m\}$ are expanded in time using order six B-splines $M_n(t)$, so that:

$$g_l^m(t) = \sum_{n=1}^{6} g_l^{mn} M_n(t), \quad h_l^m(t) = \sum_{n=1}^{6} h_l^{mn} M_n(t). \tag{5}$$

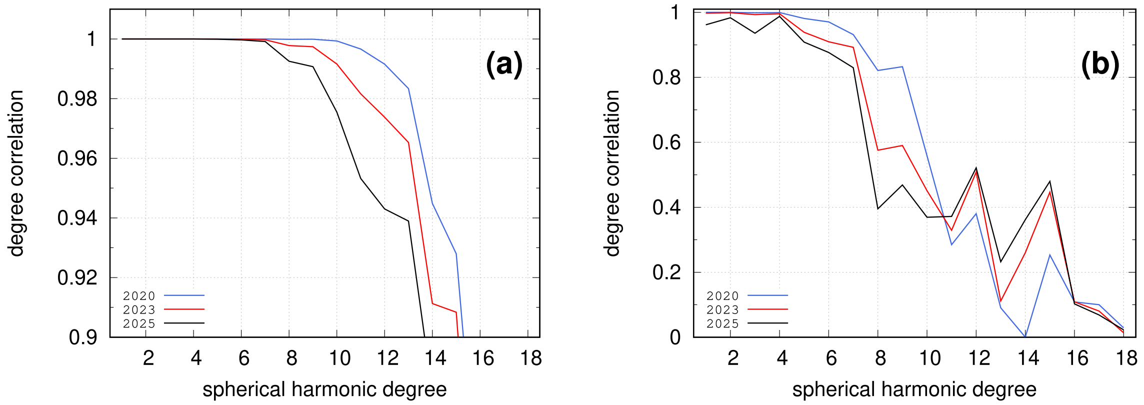

Fig. 3 Degree correlation between the models of C^{3}FM4-Z and CHAOS-7 for the main field (**a**) and the secular variation (**b**) at three different epochs. Note the different y-scales in the plots

The objective function $\Phi(\mathbf{m})$ to be minimized in the inversion is

$$\Phi(\mathbf{m}) = (\mathrm{y} - \mathbf{Am})^{\top}\, \mathbf{C_e}^{-1}(\mathrm{y} - \mathbf{Am}) + \mathbf{C_m}^{-1} + \mathbf{C}_{\mathrm{F1}}^{-1} + \mathbf{C}_{\mathrm{F2}}^{-1}, \tag{6}$$

where $\mathbf{A}$ is an operator which relates the model vector $\mathbf{m}$ containing the Gauss coefficients to the data y. $\mathrm{y} - \mathbf{Am}$ is the misfit between data and model, subject to the regularization. $\mathbf{A}$ is the (design) matrix which contains derivatives of (4) for the three-field components to derive the individual Gauss coefficients. $\mathbf{C_e}$ and $\mathbf{C_m}$ are the error and the prior model covariance matrix, respectively. $\mathbf{C_e}$ contains the errors of the measurements, at the initial step diagonal elements of $\mathbf{C_e}$ are set equally to $1/5\mathrm{nTyr}^{-1}$ for each observation, as we (initially) assume a secular variation error of $5\mathrm{nTyr}^{-1}$. These elements are re-computed at each iteration step and represent the individual misfit of observations to the model of the previous iteration step. At the last iteration step these elements represent the misfit to a model derived in a rotated coordinate system that is given (spanned) by the clean, intermediate and externally disturbed directions (Wardinski and Holme 2011; Wardinski and Lesur 2012). $\mathbf{C_m}$ is an expression of the model priors, i.e., the spatial and temporal regularization.

Here, we report solutions that are adjusted to minimize the integral of B_r^2 over the core surface $\Omega(c)$ with the radius $c = 3485$ km to obtain a spatial smooth model:

$$\int_{\Omega(c)} B_r^2 \, d\Omega = \mathbf{m}^{\top}\, \mathbf{S}^{-1}\mathbf{m}. \tag{7}$$

The matrix $\mathbf{S}$ has the diagonal elements

$$\mathbf{s}_{ll}, \mathbf{t}_{ll} = \frac{(l+1)^2}{2l+1}\left(\frac{a}{c}\right)^{(2l+4)} \quad \text{for } l = 1\ldots, l_{\max}. \tag{8}$$

Like in some previous studies (Lesur et al. 2010; Wardinski and Lesur 2012), we seek a reliable estimate of the secular acceleration. Therefore, the temporal model constraint is to minimize the integral of the third time derivative of the radial field component over the core surface and in the model period between the starting and the end times t_S and t_E (1956 and 2025):

$$\frac{4\pi}{(t_E - t_S)} \int_{t_S}^{t_E} \int_{\Omega(c)} \left(\frac{\partial^3 B_r}{\partial t^3}\right)^2 d\Omega\, dt = \mathbf{m}^{\top}\, \mathbf{T}^{-1}\mathbf{m}. \tag{9}$$

The diagonal elements of the matrix $\mathbf{T}$ are the same as for $\mathbf{S}$, and the time integral is computed using a Newton–Cotes formula of a closed type, e. g. Bode's rule (Abramowitz and Stegun 1973). Minimization of the

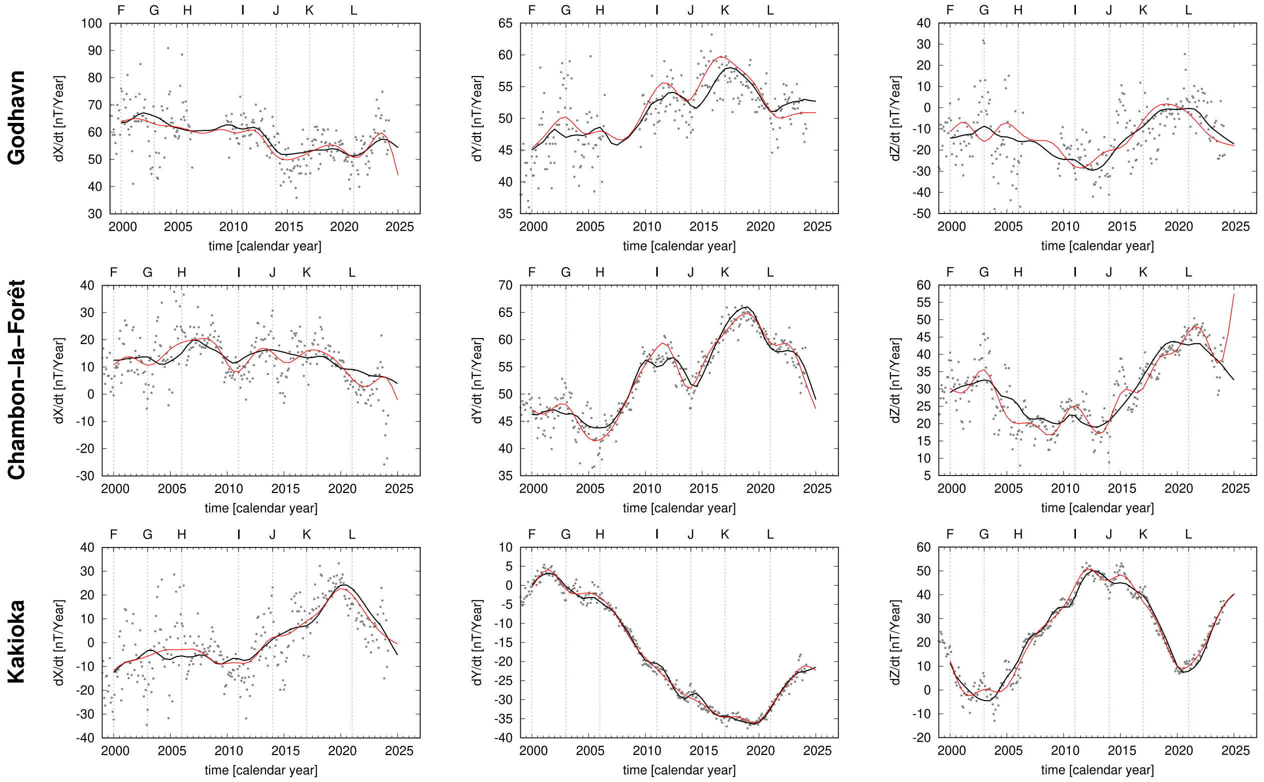

Fig. 4 The observed secular variation components at differen observatory site, CHAOS-7 (black) and the candidate parent C^{3}FM4-P (red), respectively. Gray points are the observations. Letters indicate reported geomagnetic jerks

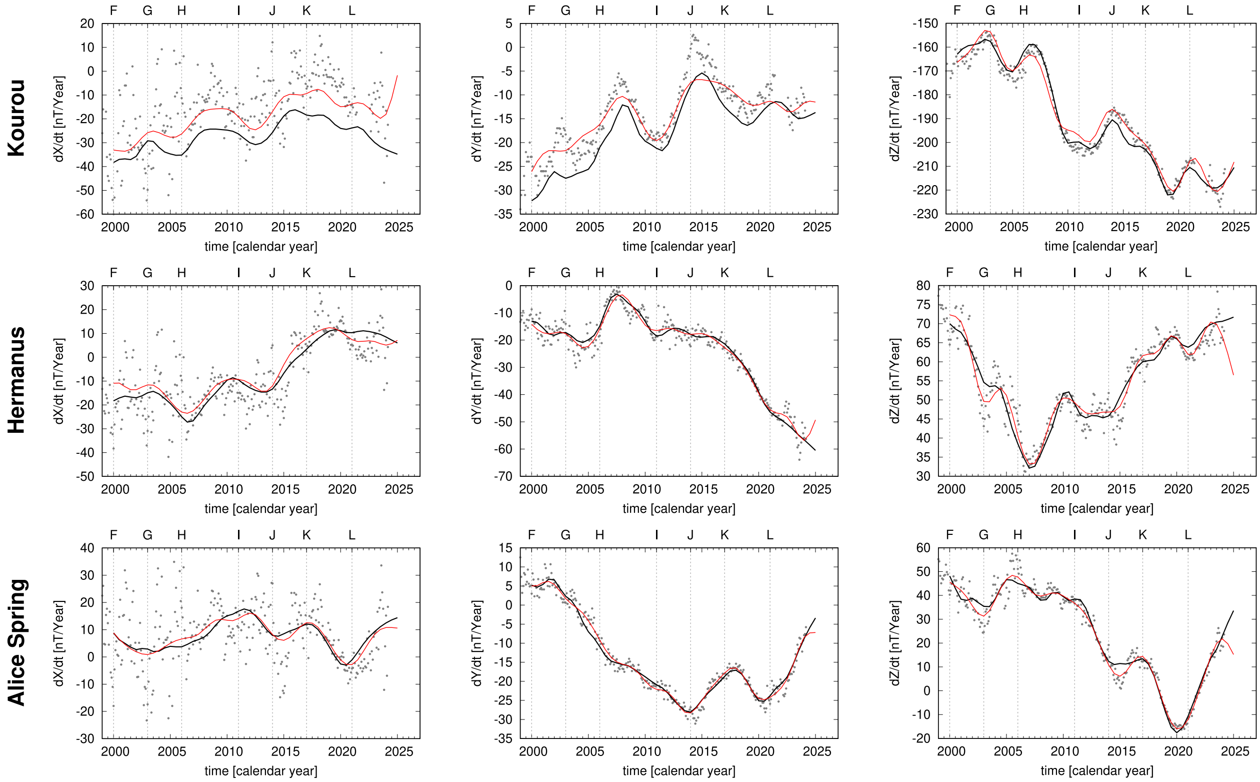

Fig. 5 As in Fig.4 for other observatories.

third time derivative requires placing further conditions on the second time derivatives of the radial field at the model endpoints; best results are obtained when these are set to zero.

The model prior covariance matrix C_m is then given by:

$$C_m^{-1} = \lambda_S m^T S^{-1} m + \lambda_T m^T T^{-1} m, \tag{10}$$

where λ_S and λ_T control the strength of the spatial and temporal constraints, respectively. The last terms of (6) are the constraints to fit given satellite field models in 2001 and 2019, which are

$$\begin{aligned}\mathbf{F}_1 &:= \int_{r=a} (B - {}^0B)^2 dS|_{t=2001} \\ &= \sum_{l=1}^{l_{\max}} \sum_{m=0}^{l} (l+1)[(g_l^m - {}^0g_l^m)^2 + (h_l^m - {}^0h_l^m)^2]_{t=2001},\end{aligned} \tag{11}$$

$$\begin{aligned}\mathbf{F}_2 &:= \int_{r=a} (B - {}^0B)^2 dS|_{t=2019} \\ &= \sum_{l=1}^{l_{\max}} \sum_{m=0}^{l} (l+1)[(g_l^m - {}^0g_l^m)^2 + (h_l^m - {}^0h_l^m)^2]_{t=2019},\end{aligned} \tag{12}$$

where ${}^0g_l^m$ and ${}^0h_l^m$ are the Gauss coefficients of the satellite geomagnetic main field model. This constraint is necessary, as our model is based on secular variation data and it needs a main field model at a given epoch in order to provide also description of the main field at all times. Traditionally, we use a main field model that is derived in an independent study from satellite data. In this study, we use a satellite-based main field model by Ropp et al. (2020). The constraint is then written

$$\mathbf{C}_{\mathrm{F}}{}^{-1} = \lambda_{\mathrm{F}} \mathbf{m}^{\top} \mathbf{F}^{-1} \mathbf{m}, \tag{13}$$

with the damping parameter λ_{F}. We choose $\lambda_{\mathrm{F1}} << \lambda_{\mathrm{F2}}$, which controls the fit to the satellite-based field models in $t_1 = 2001$ and $t_2 = 2019$, respectively. We pose a significantly weaker forcing of the model to fit a satellite field model in 2001. This is not because we doubt the satellite field model in 2001, but because that equal constraints might introduce a spurious secular variation. Such an effect was revealed by the reanalysis of the C^{3}FM (Wardinski and Holme 2006), where the equal strong forcing of the model to fit a Magsat-based field model in 1980 (Cain et al. 1989) and a Ørsted and Champ-based field model in 2000 introduced an incorrect secular variation. The very reason for this was the fundamental differences

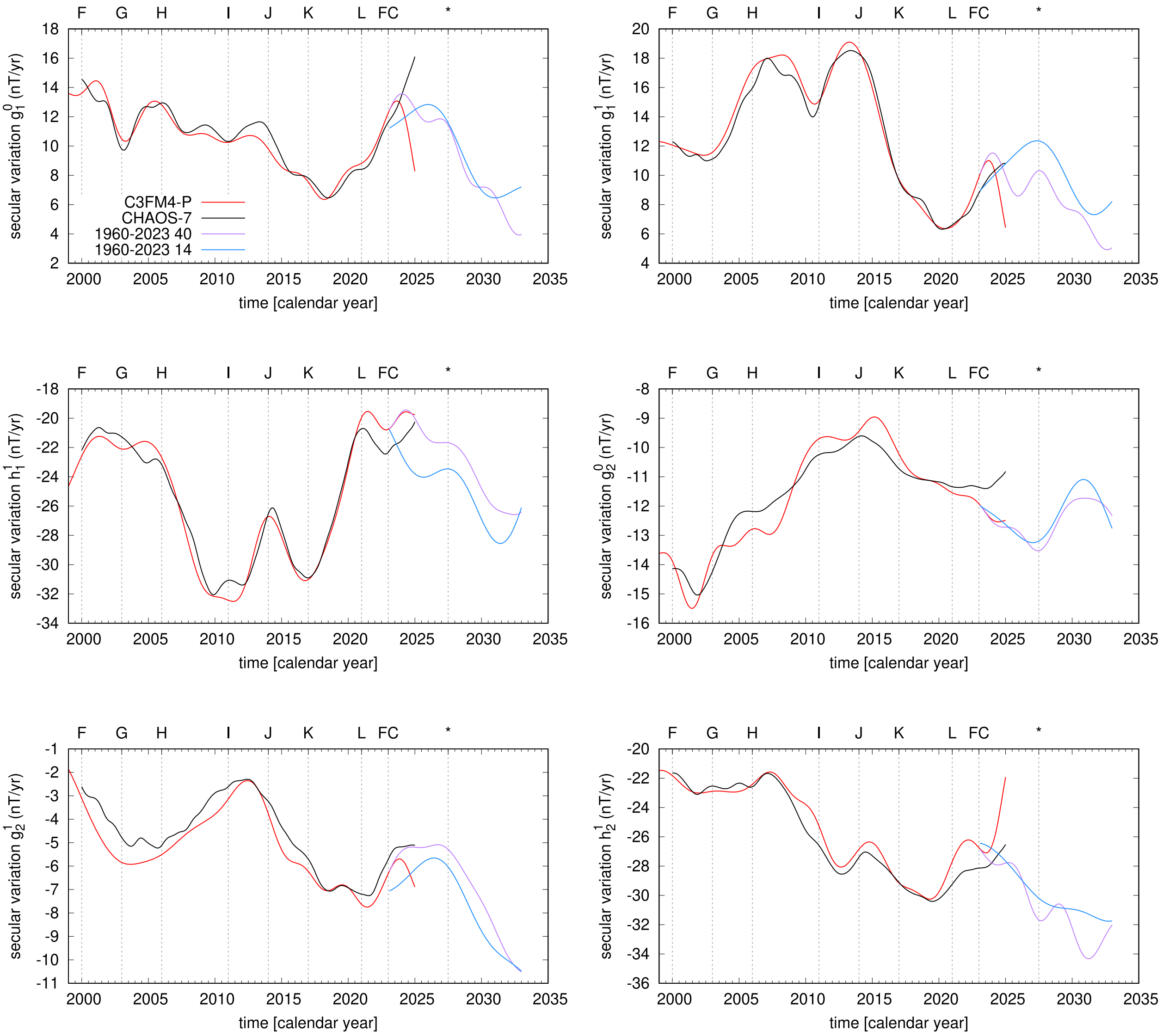

Fig. 6 Comparison of the six largest scale observed and predicted secular variation coefficients, for C^{3}FM4-P (red) and CHAOS-7 (black). Vertical line labeled as FC marks the beginning of the forecast and $*$ marks the prediction epoch for the IGRF candidate. Different colored lines represent forecasts by the MSSA truncated at 14 and 40 Eigenmodes

of the orbital geometries of the Magsat and Champ satellite missions. While Magsat was flying on a dawn–dusk orbit, Ørsted and Champ were also flying through local night time. The exclusive selection of night-time data to construct field models reduces the external field contributions in these field models significantly (Holme et al., 2003). Likely, field models derived from Ørsted and Champ differ from those of the Swarm constellation, because of their different data distribution, therefore a different forcing $\lambda_{F1} << \lambda_{F2}$ to fit these models may prevent us from introducing spurious secular variation. However, this effect was not studied in full detail.

Solutions are sought iteratively in a very similar manner as for the previous model, C^{3}FM3 (Wardinski et al. 2020), by deriving an initial model to re-weight the observatory data by their residuals to this initial model. The error matrix $\mathbf{C_e}$ of (6) is updated to derive the second-step model. Then, the influence of external field variation is reduced by a noise-removal scheme, where residual variability that correlates with the D_{ST} -index is suppressed (Wardinski and Holme 2011). This provides the second and final update of $\mathbf{C_e}$ to derive the final model.

Table 1 lists the inversion parameters of three models. C^{3}FM4-P is the parent model derived up to spherical harmonic degree $\ell_{max} = 14$. C^{3}FM4-Z results from the same inversion parameters as C^{3}FM-P, but is extended up to spherical harmonic degree $\ell_{max} = 18$. C^{3}FM4-S results from relaxing the spatial constraint and is given to spherical harmonic degree $\ell_{max} = 18$. The two latter models are derived to allow a comparison to CHAOS-7 and to study small-scale features of the secular variation.

3 Comparisons of main field and secular variation models

In this section, we provide an initial comparison of our modeling results with a satellite-based geomagnetic field model CHAOS-7. First, we analyze the spectral content of the models and their differences by computing the power spectra (Mauersberger 1956; Lowes 1966):

$$\begin{aligned} R(\ell) &= \left(\frac{a}{c}\right)^{2\ell+4} (\ell+1) \sum_{m=0}^{\ell} (g_\ell^m)^2 + (h_\ell^m)^2 \,, \\ R_\delta(\ell) &= \left(\frac{a}{c}\right)^{2\ell+4} (\ell+1) \sum_{m=0}^{\ell} (\delta g_\ell^m)^2 + (\delta h_\ell^m)^2 \,, \end{aligned} \tag{14}$$

where $\delta g_\ell^m = \check{g}_\ell^m - g_\ell^m$ and likewise δh_ℓ^m are the differences of the compared models. Similarly, (14) can be applied to the spherical harmonic coefficients of the secular variation and their differences.

The spectral content of the compared models and their spectral differences for three epochs are shown in Fig. 2. The spectral curves of the main field match each other until $\ell = 13$ and then start to deviate. The spectral power of their differences is smaller than the power of the main field itself for $\ell < 14$. Their spectra and those of their differences do not intersect for $\ell < 14$. The largest deviation is displayed for the epoch 2025, where the versions of C^{3}FM4 are not controlled by data, but by the combination of inversion constraints. The main field power of CHAOS-7 becomes flat from $\ell > 13$, while the power of the C^{3}FM4-Z decreases. The flattening of the CHAOS-7 power is due to the crustal magnetic field, which is expected to overlay the core signal from $\ell > 13$ onward. The decaying of the C^{3}FM4-Z main field power may be attributed to the removal of crustal signals by the derivation of the secular variation data, where the constant crustal signal cancels out at each observatory location for different epochs. Therefore, our models do not contain signals of the crustal magnetic field.

The secular variation power spectra (Fig. 2b) start to deviate for $\ell = 7$. For degrees $\ell = 8 - 14$ the power of the secular variation from C^{3}FM4-Z (and C^{3}FM4-P) is higher than from CHAOS-7. We will discuss this runup of the secular variation power in a later section. At degree $\ell = 14$ both powers intersect and the secular variation power of CHAOS-7 becomes stronger. However, we note, that relaxing the spatial constraint λ_S by a factor of 70 (model C^{3}FM4-S) shifts the intersection of secular variation spectra to higher degrees, $\ell = 16$ (not shown).

Furthermore, we derive the degree correlation function (Toksöz et al. 1969; Arkani-Hamed et al. 1988) to gain a qualitative comparison of the two models. The degree correlation, $r(\ell)$, between the two models is defined as:

$$r(\ell) = \frac{\sum_{m=0}^{\ell} (\check{g}_\ell^m g_\ell^m + \check{h}_\ell^m h_\ell^m)}{\sqrt{(\sum_{m=0}^{\ell}[(\check{g}_\ell^m)^2 + (\check{h}_\ell^m)^2])(\sum_{m=0}^{\ell}[(g_\ell^m)^2 + (h_\ell^m)^2])}}. \tag{15}$$

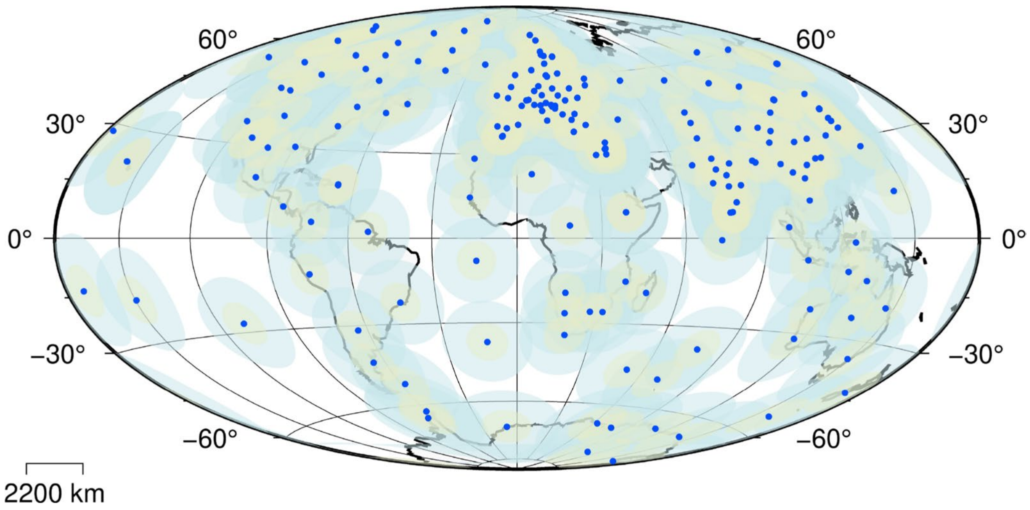

Fig. 7 Spatial coverage of the secular variation observation at Earth's surface, assuming cones of visibility with angles of 15 degree (yellow) and 30 degrees (blue). The scale represents 2200 km at Earth's surface, that represent the corresponding to a spherical harmonic degree of $\ell = 18$.

The degree correlations of the two main field and secular variation models are shown Fig. 3. The main fields are fairly similar with the degree correlation is greater than 0.9 for spherical harmonic degrees $\ell \leq 14$. However, when compared to similar Figures derived during the previous evaluation of IGRF candidate models (Alken et al. 2021b) the degree correlation is mostly higher than 0.95 among satellite-based models. This could be explained by our processing of the observatory data, where the derivation of secular variation estimates removes the crustal signal, as it should be constant with time and is expected to dominate the core signal for $\ell \geq 13$.

The degree correlation of the secular variation indicates that the models deviate largely for $\ell > 6$. Again, relaxing the spatial constraint allows for more spatial details of the secular variation of C^{3}FM4-S which deteriorates the degree correlation of the secular variation for these degrees largely (not shown). The weakest correlations are found for the epoch 2025, where no secular variation data from ground-based geomagnetic observatories were available at the time of the model derivation, and the model is controlled by the priors and particularly by the end-point constraints for which the second time derivatives of the radial field are set to zero at 1956 and 2025.

Figures 4 and 5 compare modeled and observed secular variation at different geomagnetic observatory sites. We choose six sites with long and continuous records to represent the northern and southern hemispheres. Shown are the three secular variation components for the period 2000 to 2025 to allow an easy comparison. Vertical lines mark reported geomagnetic jerks (Brown et al. 2013; Torta et al. 2015; Whaler et al. 2022) and also the postulated jerk for 2020/2021 (Wardinski et al. 2020; Pavón-Carrasco et al. 2021). Largest differences in all three components between the model and the observed secular variation are found at Godhavn (Greenland) in the north polar region. Here, signals of short-term external field variations dominate the secular variation. For the other observatories, deviations of a few tenths of nT/year are found for at least one component of the observed secular variation, mostly in dX/dt. The larger amplitude of residuals in the dX/dt component can be explained by the geometry of the magnetospheric ring current that causes an additional northward directed magnetic field. These contributions are of external origin and therefore not described by our models.

The secular variation of the two models mostly agree with each other, particularly, in Europe, East Asia, Australia and Africa. Some differences can be seen in Godhavn and in the dX/dt and dY/dt of Kourou (French Guyana). CHAOS-7 seems to show temporal details and captures some of the fainter geomagnetic jerks, for instance the ditch of dY/dt in Chambon-la-Forêt (CLF) at 2011. In the other two components at CLF actually our model shows more temporal details. However, we also note differences of the two models at the model endpoint, where their trends diverge. This is most likely due to different constraints of the model third time derivative at the endpoints. Most interestingly, both models equally describe the very strong secular variation of the vertical component that is seen at the Kourou observatory, possibly related to the South Atlantic Anomaly. Such strong secular variation is unseen in direct observations of the geomagnetic field during the past centuries (see for instance Jackson et al., (2000)).

4 Secular variation forecasts

Our forecasting strategy follows closely that of the derivation of the previous IGRF candidate (Wardinski et al., 2020), where multi-variate time series models of secular variation coefficients are built from a multi-variate singular spectrum analysis (MSSA) (Broomhead and King 1986; Plaut and Vautard 1994; Wardinski et al. 2020). The method avoids the implicit assumption about the time series stationarity which is unlikely for the temporal variability of the geomagnetic field (Hulot et al. 2010). The analysis considers discrete series of secular variation coefficients

$$y_t := \dot{g}_\ell^m(n), n = 1, \ldots, N \tag{16}$$

consisting in N observations regularly sampled in time. The sampling time τ_s is chosen to be one month. The multi-variate singular spectrum analysis decomposes the temporal variability of the series in Eigenmodes (Vautard et al. 1992; Golyandina et al. 2001; Ghil et al. 2002). The time-series models are then reconstructions based on superposition of these Eigenmodes.

If the sample $\dot{g}_\ell^m(n), n = 1, \ldots, T$ serves as the time range for a training set, then the model parameters are estimated from these observations. The (out-of-sample) prediction is generated over the time range $T + 1, \ldots, T + h$ according to the generation mechanism of the model, i.e., the superposition of Eigenmodes. As in Wardinski et al. (2020), we consider 10 years as the time range of the prediction. This sets $h = 120$ months. Prediction models are derived using the first 22 eigenmodes obtained by the MSSA of the temporal field variability.

To avoid the influence of the model end-point constraint (11), we set the training-interval from 1960.0 to 2022.9. The secular variation forecast is initialized at 2023.0.

Different secular variation forecasts for differently truncated MSSA are shown in Fig. 6. MSSA_14 represents the forecast based on the first 14 Eigenmodes and MSSA_40 is based on 40 Eigenmodes. Generally, a

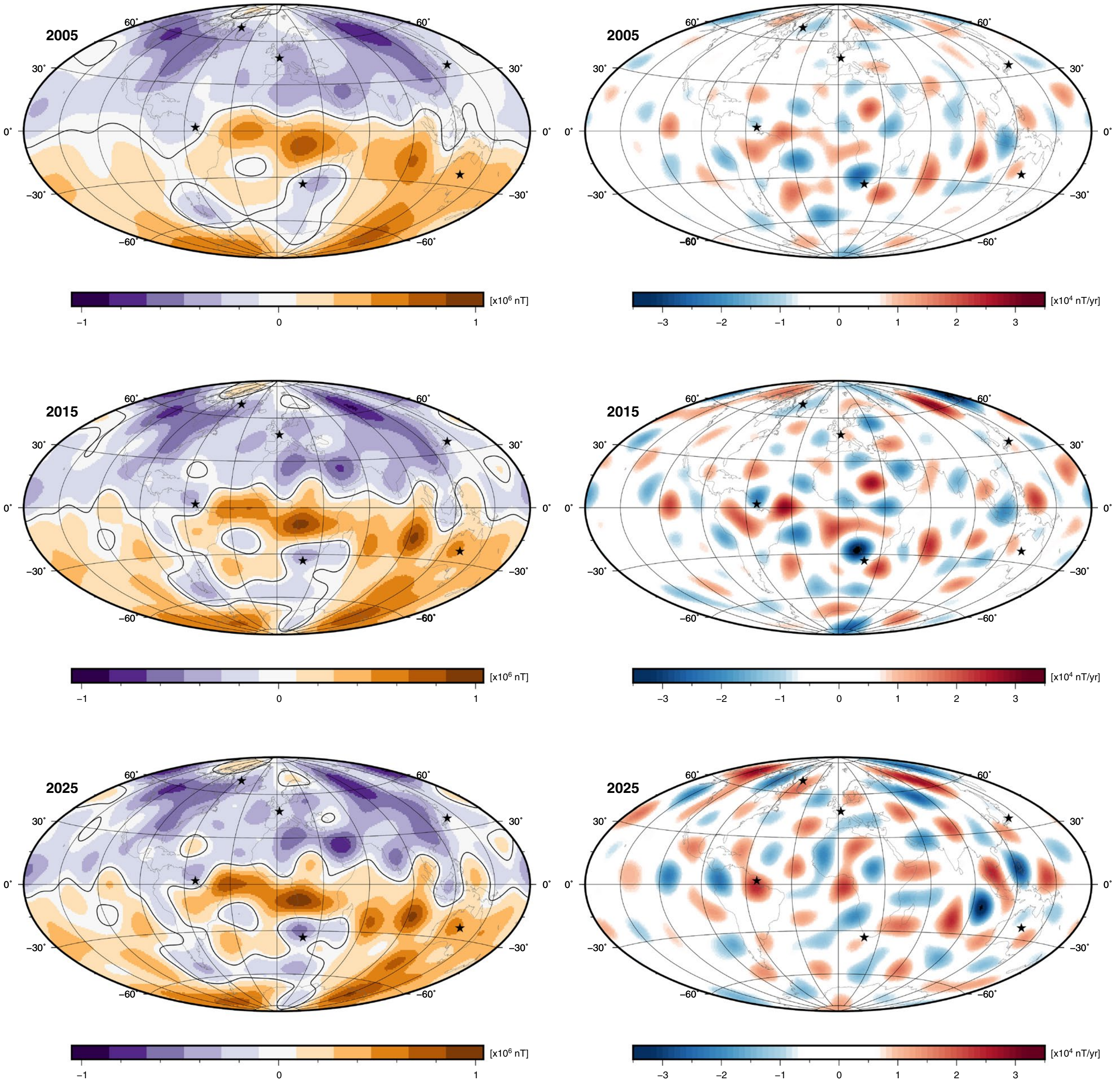

Fig. 8 Left, the radial component of the magnetic field at the core surface. Right, the radial component of the secular variation at the core surface. Black stars mark the observatory locations for which the modeled and observed secular variation are shown in Figs. 4 and 5. The $B_r = 0$ contour is shown in black in the radial field maps

higher number of Eigenmodes captures more variability of the secular variation over the training interval, where the strength of the Eigenmode decreases with increasing numbers. For instance Eigenmode 14 represents ~ 0.5 % of the total variability of the secular variation. Or, in other words, the variance reduction of the residuals derived from the fit of the MSSA to the observation (training data) is almost constant from MSSA degree 14. A closer inspection indicates discontinuities of a few nT/yr at the beginning of the forecast (marked as FC in Fig. 6) mostly visible between the red and blue curves in the forecasts of the secular variation coefficients g_1^1, g_2^1. The cause for these discontinuities is not clear, but might be related to the gap of one month between the end of training and the beginning of the forecast.

Plots of the secular variation coefficients (Fig. 6) show a strong oscillation towards the endpoint for some coefficients. We can note a different behavior of CHAOS-7 and C^{3}FM4-P close to the model endpoint, particularly clear for g_1^0 where curves of the two models continue in

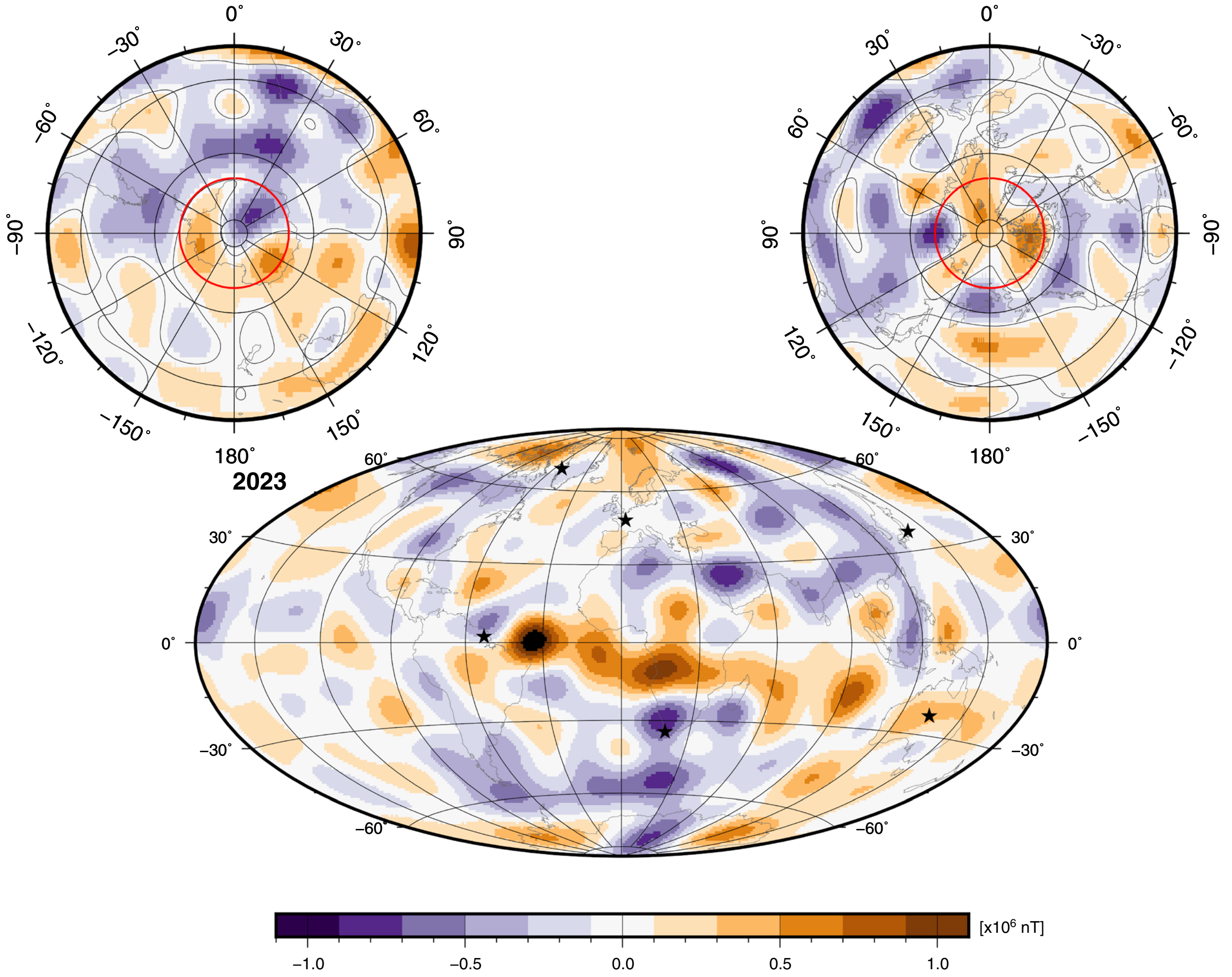

Fig. 9 Maps of the radial component of the non-dipole magnetic field at the core surface, which is computed from spherical harmonic degrees 2–18 of C^{3}FM4-S in 2023. South and North polar views are given above with red contours marking the tangent cylinder. Black stars mark the observatory locations for which the modeled and observed secular variation are shown in Figs. 4 and 5

opposite direction. According to CHAOS-7 the dipole decrease will accelerate, whereas according to C^{3}FM4-P it will to decelerate. This is caused by the application of the endpoint-constraint in the derivation of C^{3}FM4-P, and it displays an imbalance between data availability and the objective of the constraint to minimize the secular acceleration. Without data the constraint cannot be balanced. This is the reason why forecasts are initialized 2 years prior to the model endpoint.

5 Results and discussion

In this section, we present results of the core field modeling and the secular variation forecasts. We mainly discuss findings during the satellite era, i.e., 2000–2023, to ease the comparison with satellite-based field models. At the end of this section, we describe the derivation of our candidates for the definitive geomagnetic reference field model (DGRF) in 2020, the IGRF candidate model for 2025 and the secular variation forecast for 2027.5.

5.1 Models comparison

Before we discuss models comparison, we would like to explain why the distribution of geomagnetic observatories may allow assessments of small-scale secular variation at $\ell \geq 14$. Our reasoning is based on results of Hammer and Finlay (2019), where observed secular variation at satellite altitude represents a spatial average of the secular variation within a section at the core surface. We assume this applies also for geomagnetic observatories. Figure 7 shows the spatial coverage of secular variation observations at Earth's surface for differently sized circular areas at the core surface. Here it is assumed that the secular variation signal is transmitted through the non-conducting mantle. It will be observed directly

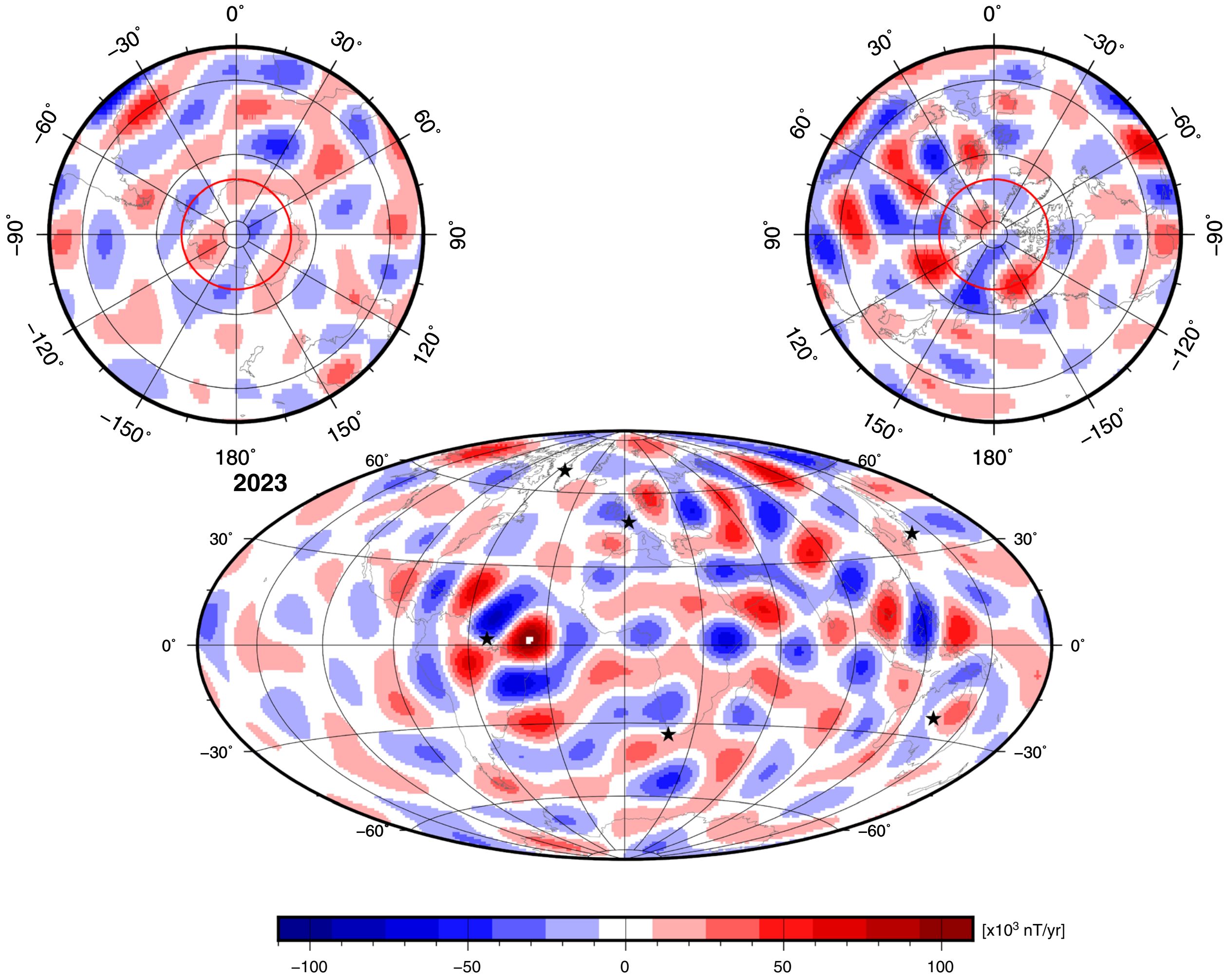

Fig. 10 Maps of the radial component of the non-dipole secular variation at the core surface of the C^{3}FM4-S in 2023. South and North polar views are given above with red contours marking the tangent cylinder

above the point where it is originated, but also at a distant point away from the central point. We characterize the distant point by an angle α of 15 degrees (yellow in Fig. 7, corresponding to a pessimistic view) or 30 degrees (blue in Fig. 7, corresponding to an optimistic view). The diameter of the cone is given by:

$$d_{\mathrm{cone}} = 2 \cdot h \tan(\alpha), \tag{17}$$

where h is distance from the core surface to Earth's surface. For simplicity, we assume both circular areas created by the projection of cones to be perfect. Figure 7 reveals a good coverage of secular variation observations in the northern hemisphere, but also voids in the observatory networks with uncertain secular variation observations, particularly in the Pacific ocean. The maximum distance between neighboring circular areas to allow the resolution of secular variation of a given ℓ can be estimated by:

$$\Lambda \sim \frac{2\pi r_E}{\ell}, \tag{18}$$

where $r_E = 6371.2$ km is Earth's reference radius. For $\ell > 14$ we find Λ to be smaller than 2800 km. Secular variation features of $\ell = 18$ limit the maximum distance Λ to be smaller than 2200 km at the core surface. We use 2200 km as scale in Fig. 7 to ease the identification of regions for which the observatory coverage is not sufficient to resolve very small-scale secular variation. Indeed, the observatory coverage should allow the recovery of small-scale secular variation to a high degree for most of the global regions, except under the Pacific and regions in southern Indian and Atlantic oceans. It should become evident that spatial gaps in the observatory distribution will aggravate our knowledge on small-scale secular variation on decadal and centennial timescales.

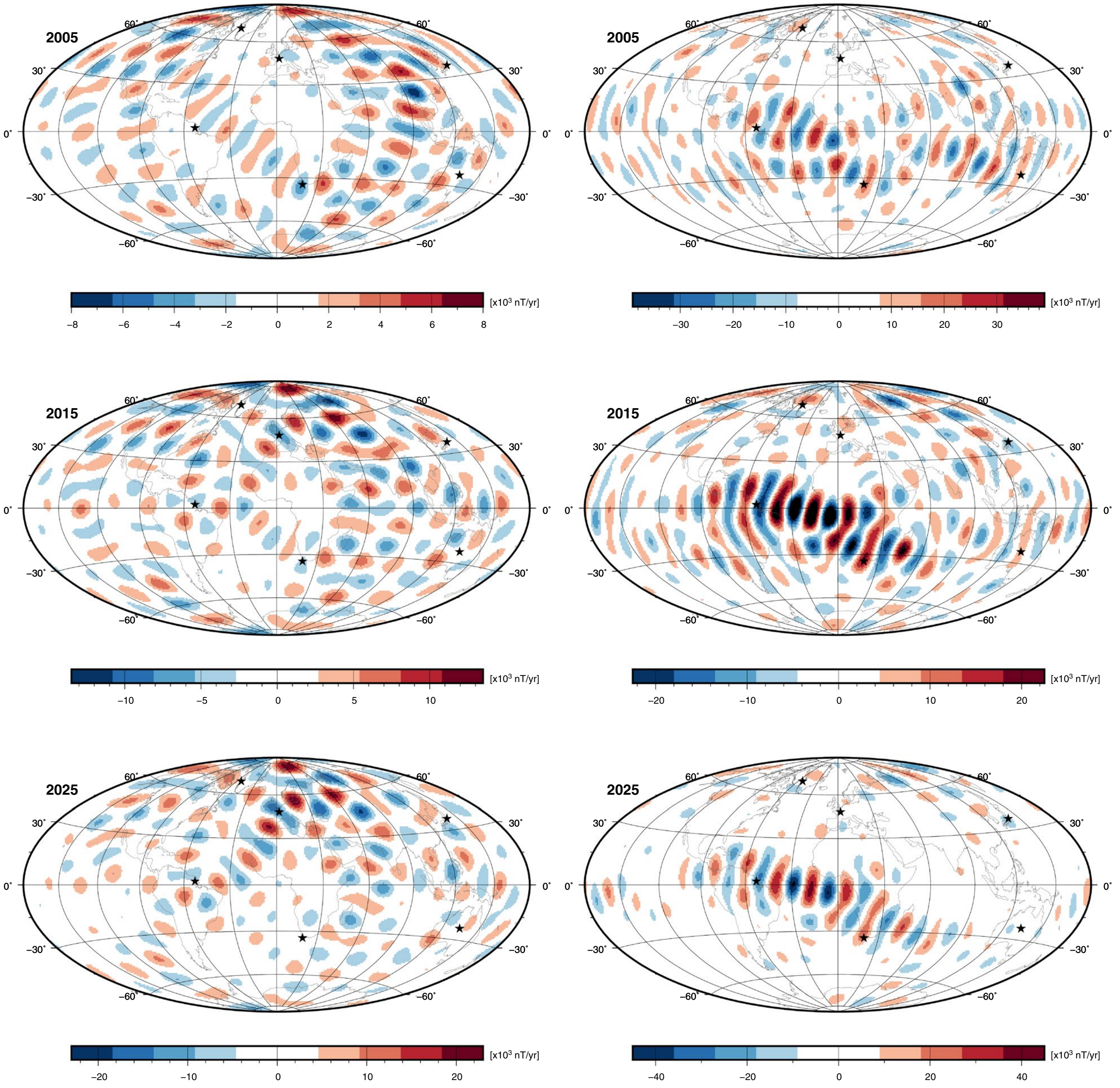

Fig. 11 Maps of the small-scale secular variation (degrees 14–18) of the radial field at the core surface. Compared are maps of the C^{3}FM4-S (left) and the CHAOS-7 model (right). Note the different scales of the individual maps

After this analysis, we compare CHAOS-7 and C^{3}FM4-P models. The degree correlation highlights only minor differences between the main field models of CHAOS-7 and C^{3}FM4-P for epochs after 2020. The differences slightly reduce when C^{3}FM4-P is constrained to fit a satellite-based main field model in 2019, rather than in 2015. At maximum, these models can be considered practically identical up to spherical harmonic degree $\ell = 12 - 14$ with a correlation ~ 0.9.

The degree correlation of the secular variation differs substantially, reflecting the apparent differences of the secular variation seen in the spectra (Fig. 2b). The secular variation power of C^{3}FM4-P is higher than of CHAOS-7 at degrees $\ell = 8 - 14$. Relaxing the spatial constraint emphasizes the higher secular variation power of C^{3}FM4 at these degrees even more. The cause of the higher power in C^{3}FM4-P at these degrees needs to be explained, but, so far, we can only speculate upon reasons. The different source geometries of satellite and ground-based data may play a role: Satellite data consider every magnetic field generation below their orbital sphere to be of internal origin. This

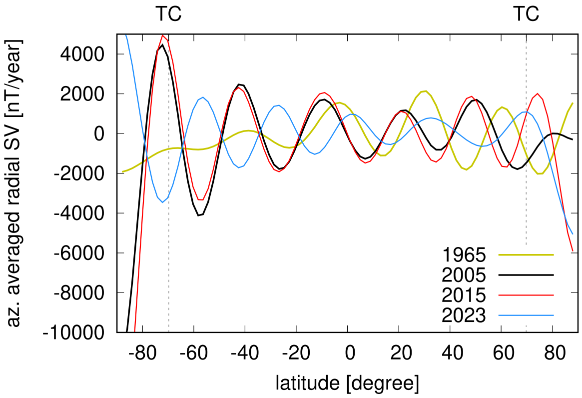

Fig. 12 Profiles of the azimuthally averaged radial secular variation at the core surface for four different epochs. TC marks the southern and northern intersections of the tangent cylinder and the core surface

might be erroneous as night-time and quiet-time ionospheric field generation may also map into these data as internal sources, whereas in ground-based observatory data these may be regarded as external sources. On the other hand, ground-based data are closer to the source of secular variation, but may also sense external and externally induced magnetic field sources.

5.2 Maps of the radial field and its secular variation

Maps of the radial component of the magnetic field and its secular variation at the top of the core are shown in Fig. 8. The radial magnetic field (Fig. 8 left) shows a dipole-dominated morphology, but with considerable small-scale features, such as reversed flux patches in both hemispheres. For the period from 2005 to 2025 we observe a growth of two reversed flux patches in the North polar region and the opening and widening of the corridor that connects the inward flux of the northern hemisphere and the reversed flux under the South Atlantic. A westward drift of the field features can also be seen for this period, see e.g., the intense outward flux patches below South Africa and equatorial Atlantic.

The secular variation at the core surface (Fig. 8 right) is dominated by small scales. Particular notable features are low latitude pairs of opposite polarity secular variation features which are typical to advection (Amit 2014). Note the large bipolar pairs of intense patches of the radial secular variation at high northern latitudes, e.g., under Eastern Siberia which are consistent with a westward jet (Livermore et al. 2017). Overall the secular variation is stronger in the Atlantic hemisphere than in the Pacific (Hulot et al. 2002; Holme et al. 2011; Colas et al. 2025).

We also provide maps of the core field and the secular variation where the dipole contribution is omitted; see Figs. 9 and 10. The non-dipolar radial magnetic field (Fig. 9) shows outward intense features in the equatorial region, inward intense features below the South Atlantic related to the South-Atlantic anomaly (Terra-Nova et al. 2017) and normal polarity patches centered around the edges of the inner core tangent cylinder. These latter features aligned with the inner core tangent cylinder were used to infer the size of Mercury's inner core (Wardinski et al. 2021). In the northern hemisphere the patches are slightly outside the tangent cylinder whereas in the southern they are inside the tangent cylinder. The northern high-latitude normal flux patches are more intense than the southern, resulting in larger amplitude of polar minima in the north (Lézin et al. 2023). Close to the locations where intense flux features in the core exist (Fig. 9) often intense secular variation features exist (Fig. 10). Most noticeably underneath the North polar region and North-east Brazil which may imply either rapid advective motions or shearing (Terra-Nova and Wardinski 2023).

Figure 11 shows maps of the small-scale radial secular variation derived from the C^3FM4-S and the CHAOS-7 models related to the Gauss coefficients from spherical harmonic degrees $\ell = 15 - 18$. First we notice that the intensity of the features derived from C^3FM4-S is weaker than of the features in CHAOS-7 model. This might be explained by the strength of the spatial damping, λ_S. Relaxing this may yield stronger features. Further, we notice the different orientations of the features of the two models. Broadly, the features of C^3FM4-S align in north–south direction, whereas features of the CHAOS-7 model align in east-west oriented features are persistently seen in the three epochs of Fig. 11. Strongest features of C^3 FM4-S appear in the Eurasian section, close to North pole, while the strongest features of the CHAOS-7 model exist in the equatorial region under South America and Africa. These features of CHAOS-7 may not be robust, and are likely introduced by the regularization in the derivation of CHAOS-7 (Finlay. C. C., personal communication 2025). Both models show intense features for 2005 underneath East India, but apart from these no further features can be identified commonly. This is also reflected by the secular variation degree correlation, which is mostly below 0.5 for these degrees (see Fig. 3).

We also plot profiles of the azimuthally averaged radial secular variation; see Fig. 12. The epochs 2005 and 2015 show almost the same profile, whereas at an earlier epoch, 1965, and a later epoch, 2023, profiles largely differ. This indicates that secular variation morphology largely changed between 2015 and 2023. The significant difference of the profiles during the satellite era suggests a reconfiguration of the secular variation almost at all latitudes except inside the northern tangent cylinder. We spot several features in the maps of Fig. 8 that emerged around 2023 and that may have

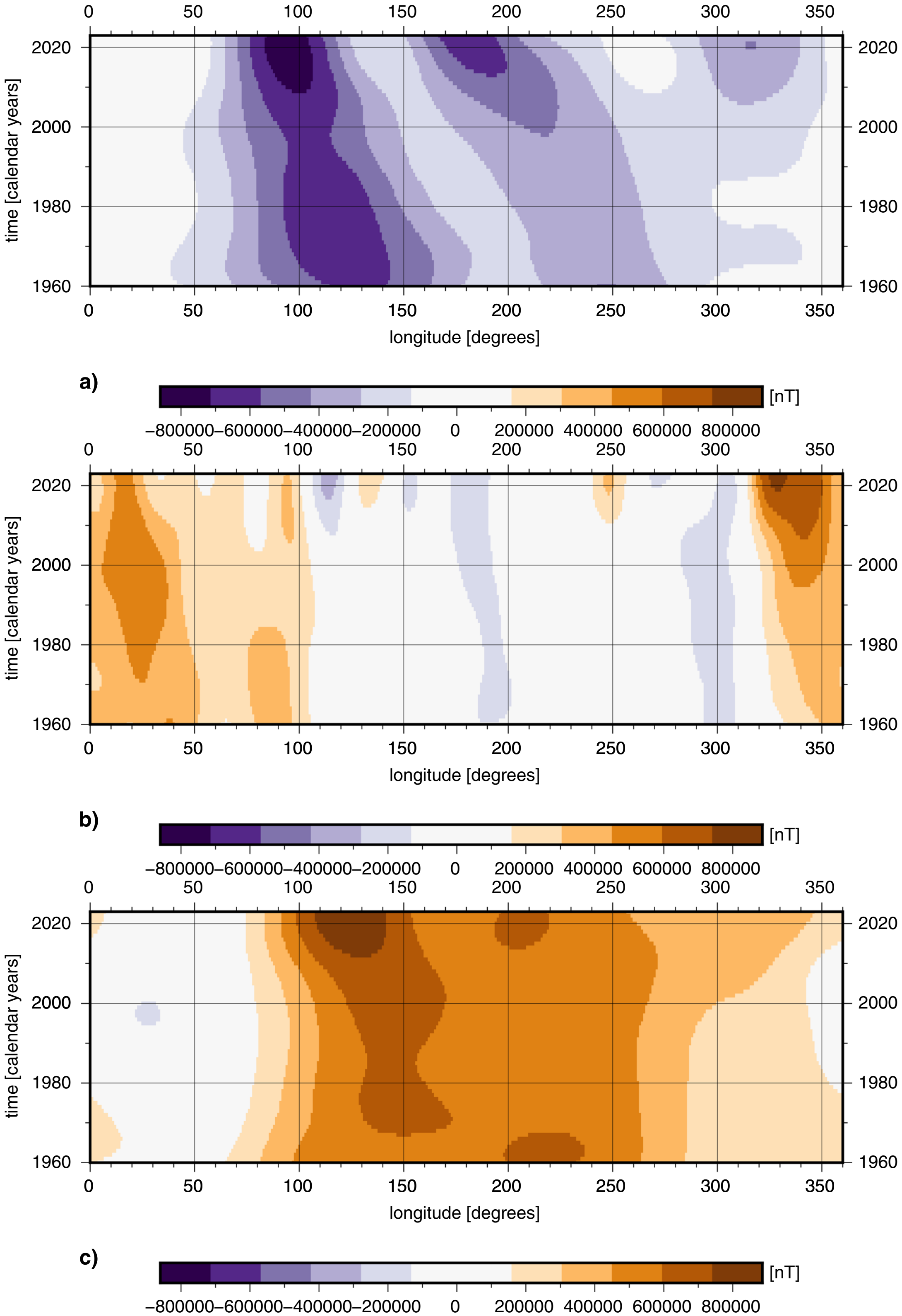

Fig. 13 Longitude–time plots of the radial component of the core field at the core surface for three latitudinal bands, **a** at the northern rim of the tangent cylinder, **b** at the equator and **c** at southern rim of the tangent cylinder

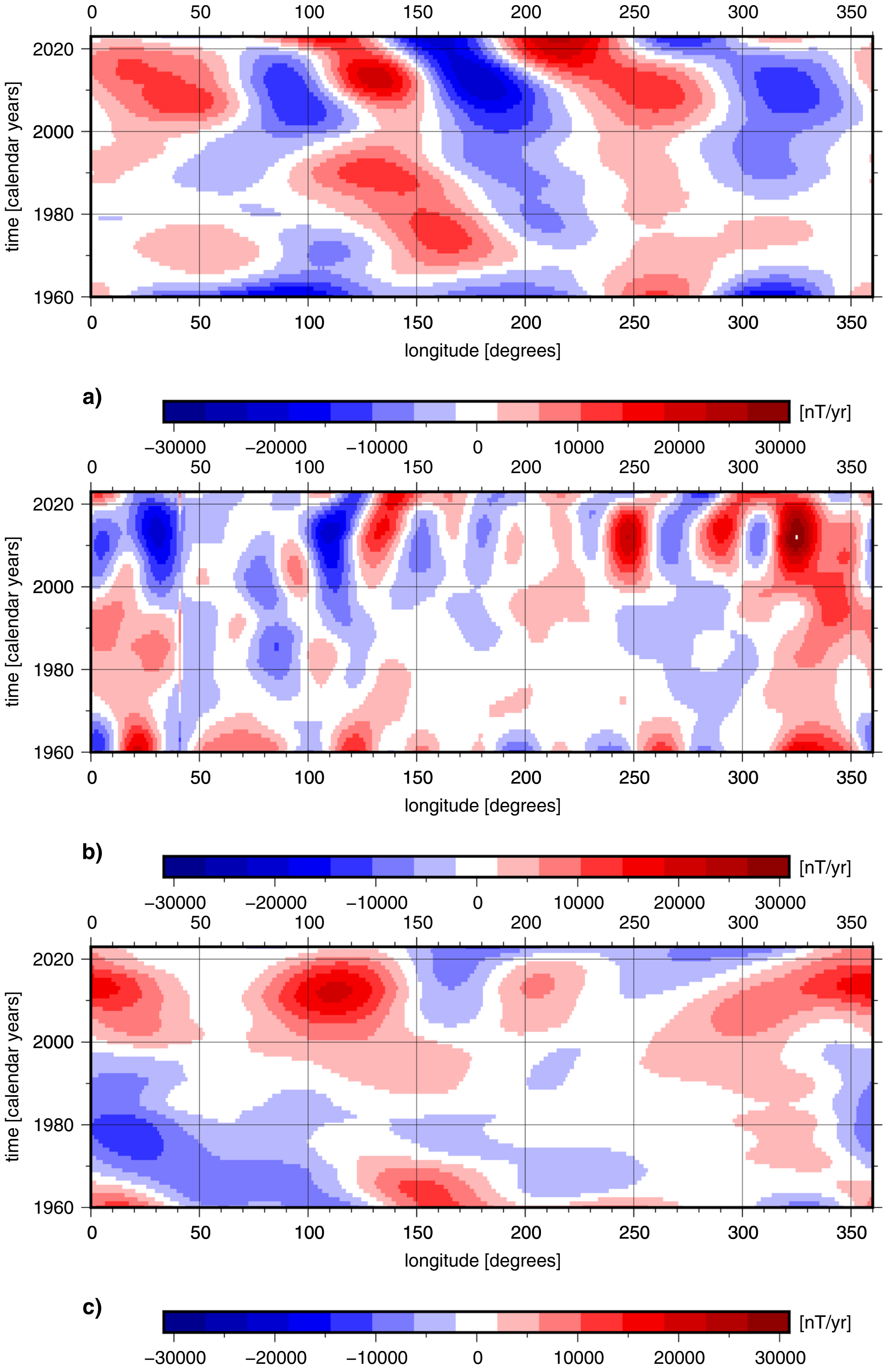

Fig. 14 Longitude–time plots of the radial secular variation at the core surface for three latitudinal bands, **a** at the northern rim of the tangent cylinder, **b** at the equator and **c** at the southern rim of the tangent cylinder

altered the shape of the profile in 2023, substantially. For instance the two blue patches west of South America, or the re-organization of patches inside the southern tangent cylinder. In this context, Lesur et al. (2022) reported short lived secular acceleration features that occurred between 2015 and 2020 at the equator and which drifted westward by 20° until 2020. We note the off-phase relation between the 2023 zonal profile to those of 2005 and 2015. This off-phase strongly indicates meridional motion of field features.

Both maps (Figs. 8 and 11) and zonal profiles (Fig. 12) at different epochs indicate that the secular variation throughout the model period underwent considerable changes. An efficient way to represent azimuthal displacements of magnetic field features at a given latitude were proposed by Finlay and Jackson (2003); Dumberry and Finlay (2007). We apply these longitude–time plots to the radial component of the core field and its the secular variation; see Figs. 13 and 14. We select three latitude bands, both intersections of the tangent cylinder with the surface of the outer core and the equator, as these regions may accommodate different types of geodynamo actions (Christensen et al. 1998; Aubert et al. 2008).

Radial field features in Fig. 13a and c are slightly tilted, which can be interpreted as a westward drift of these features, as proposed by Finlay and Jackson (2003); Dumberry and Finlay (2007). This westward drift signature is particularly evident at the edge of the northern tangent cylinder.

Similarly, this can be drawn from the longitude–time plots of the secular variation of the radial field. A westward motion of the secular variation features in Fig. 14a and c can be concluded from tilted red and blue bands in the map. Secular variation features in the equatorial region do not show an apparent azimuthal motion, rather a varying intensity of features with time (Fig. 14b), which might be interpreted as signatures of standing waves. Moreover, we note that the Pacific region shows an episode of very weak secular variation during 1960–2000, and then a recent strengthening.

5.3 Derivation of candidate models

Now, we want to outline the derivation of candidates models for the IGRF-14. Our candidate models for the DGRF 2020, IGRF 2025, and the secular variation for the period 2025 to 2030 are derived from C^{3}FM4-P and its respective forecast. We derive the candidates for the DGRF 2020 and IGRF 2025 by the main field model in 2020.0 and 2025.0, respectively, truncated at spherical harmonic degree 13, in nT with two decimal places. The candidate of the secular variation model is given by the forecast for the epoch 2027.5 which is meant to represent the secular variation between 2025 and 2030 truncated at spherical harmonic degree 8.

6 Conclusion

We derive a set of three continuous field models for the period 1956 to 2025 from ground-based geomagnetic observatory data. The models present the geomagnetic field, its secular variation and acceleration and are constructed using a classical field modeling approach that provides an optimal fit to secular variation observations. By fitting the models to satellite-based main field models in 2001 and 2019, they also model the core field for the period 1956 to 2025. The three individual models differ by their maximum spherical harmonic degree ℓ_{max} and the strength of the spatial smoothness constraint in their derivation. C^{3}FM4-P from which we determine the IGRF candidates is derived up to $\ell_{max} = 14$, C^{3}FM4-Z is derived to $\ell_{max} = 18$. C^{3}FM4-P and C^{3}FM4-Z are identical up to $\ell = 14$. The third model, C^{3}FM4-S, is also derived to $\ell_{max} = 18$, but the spatial constraint is significantly relaxed to attribute more spectral power to the Gauss coefficients, particularly to those of spherical harmonic degrees $\ell = 14 - 18$.

In this study, we apply forecasting schemes that rely on analyses of multi-variate time series (MSSA) of all secular variation coefficients from the C^{3}FM4-P model between 1960 and 2023. Time series models of the field variability are derived for different numbers of Eigenmodes of the multi-variate series. The maximum number of 14 Eigenmodes of the time series models are shrewdly selected to perform 10-year forecasts of the secular variation coefficients. The forecast of secular variation coefficients for 2027.5 presents our candidate for the secular variation for the period 2025 to 2030.

To evaluate the acceptance of our core field and secular variation models, we compare them to the satellite-based CHAOS-7 model. The comparison reveals a large similarity between the core field of CHAOS-7 and our models. There are differences in the secular variation between our model and CHAOS-7 for $\ell \geq 7$. This could be due to insufficient data coverage by ground-based geomagnetic observatories. However, Fig. 7 demonstrates that the data coverage is sufficient, and that only a few regions are not covered. Alternatively, the small-scale secular variation of CHAOS-7 might not be robust due to the applied model regularization. Our core field models indicate a recent intrusion of the magnetic equator (Fig. 8). Profiles of azimuthally averaged radial secular variation display an off-phase zonal secular variation for different epochs (Fig. 12) that can be interpreted as a strengthening of meridional core flow. Based on the discussion of Fig. 7, we note that a decimation of geomagnetic observatories will cause a loss to our understanding of geophysical processes in Earth's core on decadal as well as other time scales.

Appendix A: Observatory statistics

See Table 2.

Table 2 Observatory statistics, i.e., number of secular variation estimates (N_x, N_y, N_z), mean deviation (m_x, m_y, m_z) and standard deviation $(\sigma_x, \sigma_y, \sigma_z)$ from C^{3}FM4-P for the individual components. The observatory code follows the BGS-naming of observatories which are listed in alphabetical order

Observatory code	N_x	m_x	σ_x	N_y	m_y	σ_y	N_z	m_z	σ_z
AAA	570	0.49	12.97	570	0.26	7.21	570	0.17	7.28
AAE2	585	3.29	17.88	585	−0.36	11.81	585	0.52	13.28
ABG	813	−1.00	21.55	813	0.24	7.91	813	−0.81	19.29
ABK	736	0.19	10.81	736	0.18	4.08	736	0.61	9.82
AGN	147	−1.44	10.61	147	0.00	4.88	147	0.82	12.08
AIA	710	−1.45	7.38	710	−0.25	3.16	710	0.28	6.21
ALE	420	−1.12	15.24	420	−0.01	15.94	420	−1.02	30.01
ALM	63	3.72	9.64	63	0.19	5.04	63	2.15	9.91
AML	129	0.70	8.51	129	0.25	4.69	129	0.12	6.92
AMS	345	0.82	10.61	345	−0.05	2.51	345	−0.51	6.35
AMT2	64	−3.18	10.02	64	0.28	3.66	64	−1.46	6.27
AMU	6	1.99	18.65	6	−0.05	8.95	6	−20.49	13.22
ANC	4	−3.52	54.61	4	3.38	10.55	4	2.68	9.84
ANK	7	3.62	20.33	7	72.35	82.33	7	3.15	17.35
ANN	420	−1.01	23.92	420	−0.68	24.85	420	6.77	25.79
API	743	−1.09	16.57	743	0.10	7.25	743	−0.24	7.22
AQU	588	0.53	9.86	588	−0.22	3.63	588	0.95	6.12
ARC	173	−1.99	10.85	173	−1.96	12.24	173	−0.20	7.90
ARK	36	7.03	11.38	36	0.36	3.86	36	4.69	8.24
ARS	477	−0.70	8.68	477	−0.28	6.72	477	1.30	6.44
ASC	333	5.04	11.88	333	−0.31	3.37	333	0.10	2.21
ASH	359	1.47	13.86	359	−0.42	8.53	359	0.53	12.63
ASO	18	6.56	15.29	18	−2.05	2.17	18	−4.84	6.09
ASP	366	0.19	9.98	366	−0.06	1.68	366	0.32	3.34
AVE	2	7.67	1.08	2	−1.96	2.33	2	−0.40	0.01
BDE	6	−6.67	9.83	6	2.96	8.84	6	14.12	12.95
BDV	526	−0.06	7.83	526	0.07	2.68	526	−0.12	5.65
BEL	693	−0.19	7.34	693	0.48	3.03	693	0.00	5.51
BFE	624	−0.43	6.98	624	−0.42	3.04	624	−0.59	6.86
BFO	179	−0.33	5.10	179	−0.34	2.03	179	0.62	3.28
BGY	242	4.54	13.26	242	−1.52	7.63	242	2.58	6.64
BGY2	5	6.56	5.56	5	−0.33	0.92	5	0.81	2.39
BIN	17	0.99	13.14	17	−3.30	15.03	17	1.42	9.35
BJI	493	1.38	14.71	493	−0.12	3.07	493	−1.20	5.94
BJN2	357	−0.87	10.55	357	0.18	7.75	357	1.75	14.35
BLC	700	0.54	12.55	700	0.04	7.65	700	−1.34	18.81
BLT	6	−3.69	9.46	6	3.39	3.39	6	−1.51	10.24
BMT	322	0.52	10.37	322	−1.04	3.07	322	0.96	5.43
BNG	583	−1.94	16.91	583	−0.71	9.50	583	0.28	11.51
BOU	668	−0.05	8.82	668	0.05	2.15	668	0.77	5.94
BOX	431	0.24	8.13	431	1.11	4.30	431	−0.17	6.46
BRD	117	−2.53	6.02	117	−1.72	2.89	117	0.38	6.23

Table 2 (continued)

Observatory code	N_x	m_x	σ_x	N_y	m_y	σ_y	N_z	m_z	σ_z
BRW	706	0.15	15.52	706	0.41	10.66	706	0.08	17.84
BSL	409	1.28	31.36	409	−1.60	25.98	409	−0.78	7.23
BYR1	39	−8.83	12.88	39	−2.24	12.14	39	−6.05	29.69
BYR2	40	−0.33	13.58	40	0.25	11.48	40	1.72	14.34
CAO	4	2.00	4.80	4	−1.38	2.48	4	18.55	29.35
CBB	574	0.53	11.41	574	0.07	11.00	574	−1.01	16.86
CBI	519	−0.06	15.17	519	0.59	5.63	519	0.30	4.59
CCS	357	1.56	12.19	357	−0.61	5.88	357	2.35	24.85
CDP	241	0.43	10.30	241	−0.81	3.10	241	0.11	3.51
CKI	129	0.12	9.55	129	0.43	2.80	129	2.30	3.77
CLF	813	−0.37	8.02	813	0.08	3.59	813	0.21	5.86
CMO2	481	0.02	14.19	481	0.59	8.24	481	−1.00	14.51
CMO3	321	−0.20	11.80	321	−0.02	14.62	321	−0.82	7.46
CNB	526	0.53	9.66	526	0.25	2.82	526	−0.18	4.94
CNH1	21	0.89	6.04	21	−0.82	5.82	21	2.45	5.76
CNH2	119	−0.16	9.44	119	−0.42	2.99	119	0.52	5.91
COI	767	0.51	10.43	767	−0.26	8.28	767	−1.34	11.90
CPA	36	1.07	25.97	36	−1.28	15.09	36	3.39	47.73
CRC	4	−1.01	5.77	4	−1.10	2.62	4	1.36	9.57
CRP	168	0.83	31.69	168	−1.35	17.39	168	2.59	30.92
CSY	366	2.08	29.94	366	0.12	12.41	366	1.71	35.18
CTA	393	−0.29	12.00	393	−0.04	2.46	393	−0.04	3.88
CTS	323	−0.47	10.96	323	0.30	14.35	323	−0.88	6.50
CWE	370	2.53	13.63	370	0.98	8.82	370	0.85	11.65
CYG	57	−2.60	11.03	57	1.67	19.77	57	−4.33	15.92
CZT	492	−0.26	8.24	492	−0.14	3.97	492	0.39	5.92
DAL	104	0.71	8.51	104	0.00	1.48	104	−1.15	4.94
DED	81	−3.23	9.73	81	−1.60	6.05	81	0.95	11.65
DIK	360	0.48	12.89	360	−0.09	6.03	360	−0.19	14.93
DLN	5	2.81	11.15	5	10.16	41.44	5	0.18	2.57
DLR	283	0.15	13.01	283	0.50	5.66	283	−0.30	5.47
DLT	102	1.42	13.23	102	−10.45	35.05	102	0.11	41.07
DOB2	732	−0.05	7.68	732	−0.13	3.90	732	−0.48	7.02
DOU	802	−0.04	7.24	802	−0.01	6.34	802	0.22	8.01
DRV	575	−0.33	12.49	575	−0.48	11.57	575	3.12	28.36
DUR	12	−1.50	4.82	12	1.70	1.89	12	−1.39	2.62
DVS	150	7.15	22.36	150	1.65	18.32	150	−3.63	27.27
EBR	633	1.02	8.91	633	0.13	4.14	633	−1.20	6.25
EGS	8	−9.21	3.67	8	1.42	5.04	8	−1.33	4.67
ELT	166	0.29	12.14	166	0.76	5.22	166	−0.52	4.49
ESA	224	0.18	10.50	224	0.02	1.75	224	−0.21	3.53
ESK	813	−0.01	6.37	813	0.30	3.50	813	−0.15	6.09
ETT	35	−1.78	7.76	35	2.28	4.47	35	2.06	6.18
EYR	524	2.58	14.77	524	−4.60	23.90	524	−0.38	5.83
FAN	5	14.54	17.82	5	1.84	4.85	5	0.17	3.72
FCC	687	0.82	13.42	687	1.30	8.45	687	−0.50	15.21
FMC	12	2.81	4.33	12	6.37	3.20	12	6.34	4.18
FRD	813	0.19	9.05	813	0.23	19.05	813	−0.30	5.52
FRN	487	1.37	9.59	487	0.21	2.95	487	0.53	5.34

Table 2 (continued)

Observatory code	N_x	m_x	σ_x	N_y	m_y	σ_y	N_z	m_z	σ_z
FUQ	684	0.26	16.71	684	0.55	11.85	684	−0.54	17.87
FUR	813	−0.23	7.90	813	0.04	2.96	813	−0.00	5.60
GAN	129	0.36	11.86	129	−4.05	3.70	129	1.39	3.69
GCK	200	0.67	5.35	200	0.88	3.07	200	0.13	3.55
GDH1	228	−0.19	9.41	228	−0.56	6.13	228	−0.34	18.07
GDH2	537	0.14	8.54	537	−0.43	4.94	537	0.14	13.67
GLM	181	−0.45	10.70	181	0.49	5.97	181	0.03	4.08
GLN	151	2.18	17.27	151	−1.07	10.25	151	−2.54	11.14
GNA	672	−0.06	9.86	672	−0.05	3.55	672	−0.06	7.41
GNG	141	0.15	7.14	141	−0.64	1.81	141	−0.01	3.67
GRM	54	1.17	9.62	54	−1.06	2.91	54	−0.16	2.97
GTV	6	−4.19	6.46	6	−3.42	5.60	6	2.78	2.68
GUA	732	1.96	17.19	732	−0.01	5.22	732	0.07	5.55
GUI	337	1.07	10.22	337	0.84	3.88	337	−1.55	4.56
GWC	215	−0.68	27.51	215	−1.53	13.83	215	−0.35	16.98
GZH	605	0.90	14.72	605	−0.64	5.89	605	0.54	5.28
GZH2	5	4.29	5.63	5	0.06	0.60	5	1.98	3.39
HAD	813	−0.07	6.84	813	0.05	2.91	813	0.07	5.47
HBA	116	12.34	18.70	116	−3.29	76.22	116	−37.10	71.12
HBK	607	2.55	14.23	607	−0.65	4.35	607	−0.46	6.06
HER	813	−0.05	10.98	813	−0.13	3.44	813	−0.04	3.80
HIS	136	−0.78	11.61	136	−0.42	9.33	136	4.65	20.84
HLL	5	2.50	33.47	5	20.44	55.45	5	−370.49	1037.68
HLP	789	0.10	7.25	789	0.23	4.30	789	−0.77	6.37
HNA	20	0.40	17.43	20	−2.99	5.37	20	0.24	3.42
HON2	48	38.92	88.39	48	10.06	33.51	48	78.26	150.75
HON3	707	1.92	12.71	707	0.18	4.29	707	−0.44	4.15
HRB	813	−0.01	9.57	813	0.35	3.90	813	−0.24	7.04
HRN	528	−0.68	13.29	528	−0.11	7.80	528	0.29	15.48
HTY	259	0.26	14.46	259	−0.06	2.80	259	0.68	5.35
HUA	716	−1.50	14.39	716	−0.65	5.03	716	−0.22	3.42
HVN2	9	−0.07	10.27	9	−0.26	2.53	9	0.77	14.39
HVN3	7	−25.75	69.93	7	−11.20	16.81	7	−20.47	72.50
HVN4	3	7.74	14.58	3	−14.18	21.58	3	−11.84	11.57
HYB	523	−0.38	14.19	523	−0.59	13.32	523	−0.58	10.35
IBD	33	−2.64	18.46	33	−15.72	99.52	33	−3.38	51.85
IPM	74	−0.43	13.32	74	0.45	4.04	74	1.64	8.69
IQA	274	−0.46	22.26	274	−0.82	21.49	274	−3.32	17.87
IRT2	764	−0.86	10.55	764	−0.11	3.39	764	−1.29	8.36
ISK	465	1.69	11.94	465	0.25	4.04	465	0.72	8.59
IZN	201	1.13	8.17	201	1.79	5.71	201	0.32	7.40
JAI	217	2.42	15.24	217	−0.76	5.83	217	−0.26	6.84
JCO	172	0.80	8.39	172	1.39	6.89	172	−1.69	10.94
JRV	5	−7.29	18.13	5	−3.62	4.80	5	4.01	6.95
JSS	3	−31.82	53.46	3	−24.14	32.45	3	−97.21	95.29
KAK	813	0.19	11.94	813	−0.03	1.58	813	−0.08	3.30
KDU	325	0.50	11.77	325	−0.12	2.53	325	0.08	2.73
KEL	7	1.52	4.08	7	−2.40	2.67	7	2.05	3.53
KEP	152	0.44	5.97	152	−1.27	2.33	152	0.14	3.13

Table 2 (continued)

Observatory code	N_x	m_x	σ_x	N_y	m_y	σ_y	N_z	m_z	σ_z
KGD	255	2.12	23.91	255	0.47	16.01	255	0.44	13.44
KHB	102	2.01	8.39	102	−0.43	1.72	102	0.64	4.10
KIR	258	0.50	10.79	258	−0.85	4.51	258	0.86	12.74
KIV1	60	−2.16	14.61	60	3.51	7.44	60	−1.92	7.36
KIV2	402	0.17	8.89	402	−0.04	4.84	402	0.37	7.23
KMH	177	−0.56	8.04	177	−0.45	3.01	177	−0.23	2.90
KNY	783	0.03	12.48	783	0.12	1.52	783	−0.01	2.87
KNZ	628	0.09	12.55	628	−0.07	1.89	628	−0.14	4.44
KOD	310	−3.31	19.47	310	−0.11	15.09	310	−2.62	25.96
KOR	17	5.53	16.92	17	2.49	4.66	17	4.24	12.18
KOU	317	5.33	12.11	317	0.11	2.02	317	−0.13	3.17
KPG	64	−7.09	22.54	64	2.16	12.34	64	0.34	7.88
KRC	125	−2.03	30.90	125	9.01	28.51	125	−1.37	30.75
KSA	14	0.60	13.03	14	0.10	5.45	14	−2.52	49.43
KSH	166	−0.05	9.90	166	3.69	12.33	166	1.04	4.40
KUY	6	−1.00	30.14	6	−4.53	15.60	6	1.66	27.74
KZN	341	−0.92	11.26	341	−1.60	9.23	341	−3.85	22.00
LAS	411	−1.06	28.45	411	0.30	25.17	411	1.39	12.74
LEN	14	23.57	16.61	14	−52.20	8.71	14	−8.99	11.77
LER	813	−0.06	6.27	813	0.14	3.58	813	0.04	6.36
LGR	47	2.59	8.77	47	−0.18	3.84	47	−4.44	15.63
LIV	257	−0.20	6.52	257	−0.06	2.16	257	−0.42	4.36
LMM	154	1.33	14.61	154	1.00	9.26	154	−0.42	11.04
LNN	411	0.30	7.53	411	−1.17	4.92	411	0.36	7.29
LNP	240	−0.28	15.90	240	0.26	6.56	240	−1.01	7.42
LON	135	0.75	6.64	135	0.55	2.70	135	0.02	3.53
LOV	532	0.05	6.45	532	0.18	2.89	532	0.07	6.30
LPB	2	−5.59	7.96	2	4.14	6.29	2	69.14	25.01
LQA	119	2.70	18.26	119	0.02	4.02	119	3.91	12.29
LRM	408	−0.47	12.42	408	−0.52	6.25	408	−0.30	5.21
LRV	768	−0.09	9.75	768	0.45	4.65	768	−0.79	10.29
LSA	31	2.82	8.98	31	−1.71	3.53	31	−0.10	7.21
LUA3	96	6.17	22.34	96	0.12	11.46	96	8.35	18.98
LVV	739	1.06	10.45	739	−0.93	6.91	739	−0.76	9.68
LWI	11	4.15	12.10	11	0.55	3.31	11	0.25	2.52
LYC	153	0.54	6.13	153	1.14	2.61	153	0.71	4.96
LZH	690	0.92	13.15	690	0.16	3.87	690	−1.27	7.44
MAB	450	0.17	7.34	450	−0.02	3.14	450	−0.08	6.06
MAW	758	0.58	9.41	758	0.11	10.13	758	−1.30	18.19
MBC	407	0.24	10.62	407	0.09	10.08	407	−1.22	19.64
MBO	740	−1.57	13.93	740	0.53	3.93	740	0.26	4.61
MCP	9	−10.23	13.02	9	−15.40	10.97	9	−32.87	22.79
MCQ	813	−0.93	11.44	813	−0.44	8.77	813	−0.54	12.90
MEA	807	0.25	14.26	807	−0.05	6.75	807	−0.17	13.28
MFP	85	2.16	14.18	85	0.19	5.76	85	−0.54	3.48
MGD	485	−0.72	11.73	485	0.41	6.09	485	−2.18	14.48
MID	10	0.17	11.79	10	−0.18	2.76	10	0.22	2.78
MIR	369	−1.11	16.73	369	1.18	16.03	369	4.00	27.44
MIZ	447	0.57	12.39	447	0.04	2.25	447	−0.17	4.52

Table 2 (continued)

Observatory code	N_x	m_x	σ_x	N_y	m_y	σ_y	N_z	m_z	σ_z
MLT	41	−5.68	17.89	41	−3.56	9.67	41	10.50	46.62
MMB	796	0.27	10.97	796	−0.06	1.96	796	0.43	4.64
MMK	258	−2.21	11.24	258	−0.07	11.19	258	−3.15	16.98
MNK	468	0.33	8.91	468	−0.37	6.09	468	0.26	9.17
MOL	139	3.80	14.65	139	−0.29	10.25	139	−8.30	27.60
MOS	721	1.63	10.99	721	0.81	5.53	721	−1.60	8.99
MRI	7	2.75	22.76	7	8.54	15.76	7	−11.01	23.08
MRN	21	5.54	12.90	21	18.79	12.21	21	8.35	15.68
MUT	150	−0.11	16.43	150	0.97	11.77	150	2.88	12.66
MZL	215	−1.02	8.61	215	0.02	1.83	215	0.24	4.59
NAI	21	−0.91	8.74	21	−0.84	7.39	21	11.45	15.68
NAL	36	−0.02	9.94	36	−0.59	16.08	36	0.03	11.14
NAQ	500	−0.43	10.99	500	−0.06	5.88	500	−1.49	15.38
NCK	507	−0.66	10.16	507	0.25	6.93	507	1.13	26.03
NEW	693	−2.16	43.87	693	−0.72	12.01	693	−4.78	125.71
NGK	804	−0.09	7.09	804	0.06	2.61	804	−0.12	5.50
NGP	211	2.93	14.51	211	−2.41	18.76	211	0.36	7.93
NKK	133	2.37	12.78	133	0.20	12.94	133	−0.16	8.59
NMP2	101	4.98	15.33	101	−0.96	7.47	101	4.44	4.73
NUR	780	0.34	6.24	780	0.09	3.20	780	−0.41	6.11
NVL	193	−1.33	13.19	193	1.29	16.52	193	0.74	20.59
NVS	633	−0.87	9.64	633	−1.54	7.01	633	−0.02	6.46
OAS	6	−25.12	20.95	6	8.82	12.77	6	−7.23	11.72
ODE	572	0.50	1972.03	572	0.84	176.25	572	0.75	4171.73
ORC	100	−2.78	9.53	100	2.81	20.91	100	0.78	8.03
OTT	630	−0.07	8.67	630	0.38	3.24	630	−0.27	6.22
OUL	16	0.98	5.49	16	0.21	1.51	16	0.07	3.84
PAB	37	1.30	7.49	37	−0.63	5.46	37	0.80	4.44
PAF	664	−0.20	9.75	664	0.20	6.35	664	−0.17	6.42
PAG	788	0.69	10.27	788	0.53	3.53	788	0.22	6.83
PBQ	262	−0.15	14.12	262	−1.12	5.87	262	−0.57	12.26
PEG1	21	3.02	7.97	21	0.08	8.92	21	3.08	13.27
PEG2	104	−0.91	8.01	104	2.37	3.90	104	0.39	7.50
PET1	36	4.15	9.11	36	5.84	7.01	36	−0.84	5.50
PET2	498	−0.14	9.23	498	−0.40	4.87	498	−0.34	6.68
PHU	194	1.43	11.87	194	−0.60	4.97	194	−0.38	3.06
PIL	425	−0.19	13.16	425	0.26	3.15	425	−0.07	9.24
PIO	8	−76.16	111.94	8	4.05	41.06	8	59.70	167.74
PLR	69	−3.28	20.76	69	−1.37	6.45	69	−1.41	12.95
PMG	398	−1.62	15.08	398	0.06	3.49	398	−0.02	4.42
PND	213	−0.12	12.48	213	−3.83	13.84	213	−2.25	8.77
POD	198	0.14	10.85	198	1.43	4.31	198	−0.57	8.24
PPT	632	1.59	14.20	632	−0.42	5.67	632	0.05	4.00
PRU	42	−0.61	7.32	42	5.05	7.78	42	2.75	8.70
PST	277	2.23	9.29	277	−1.31	13.16	277	−0.13	5.63
PTU	22	−1.44	14.70	22	−11.24	21.64	22	−65.54	51.71
PTY	2	−346.98	438.29	2	29.35	39.94	2	−13.32	57.13
QGZ	98	1.42	9.73	98	0.23	3.10	98	0.66	2.94
QIX	179	−0.14	10.91	179	−0.03	1.20	179	−0.17	3.19

Table 2 (continued)

Observatory code	N_x	m_x	σ_x	N_y	m_y	σ_y	N_z	m_z	σ_z
QSB	77	3.96	13.92	77	−1.52	4.00	77	0.26	4.51
QUE	45	−2.63	22.73	45	−1.15	33.74	45	−1.11	36.56
QZH	112	−1.38	10.56	112	0.42	2.84	112	−0.79	2.78
REG	12	1.37	4.05	12	1.94	4.72	12	−0.39	5.36
RES	804	0.39	9.12	804	0.05	7.35	804	−0.20	19.16
RKT	24	−3.09	15.25	24	0.95	6.29	24	2.25	3.03
ROB	9	−7.05	18.73	9	1.31	48.99	9	1.02	24.52
RSV	300	−0.11	6.19	300	0.05	2.91	300	−0.62	6.84
SAB	393	0.69	18.75	393	−0.87	17.35	393	−0.97	34.65
SBA	686	0.37	8.97	686	0.51	11.96	686	1.48	19.09
SBL	264	−0.40	6.18	264	0.72	2.75	264	0.42	4.55
SFS1	18	6.24	9.37	18	3.22	7.49	18	2.34	50.21
SFS2	331	0.69	8.47	331	−0.17	7.72	331	0.89	4.96
SHE	136	−0.91	9.82	136	0.58	2.00	136	−0.21	1.40
SHL	108	0.26	16.60	108	9.32	16.16	108	−1.69	8.38
SHU	181	0.88	6.08	181	0.66	3.96	181	0.49	3.78
SIL	76	2.75	12.28	76	2.20	3.16	76	−0.55	7.00
SIT2	768	−0.52	9.86	768	−0.54	4.51	768	−0.66	6.99
SJG1	96	2.07	14.58	96	0.06	1.86	96	0.04	5.90
SJG2	666	−1.03	12.69	666	−0.69	3.27	666	−0.40	4.41
SJL	3	−1.17	7.63	3	0.14	4.43	3	10.43	30.07
SMG	21	−2.27	13.08	21	7.45	38.18	21	6.33	12.24
SNA1	91	−6.38	15.64	91	3.08	11.16	91	−1.54	17.52
SNA2	76	0.79	10.56	76	9.25	32.60	76	−0.42	16.83
SNA3	111	3.15	12.07	111	3.56	22.49	111	0.21	9.71
SOD3	768	−0.02	10.12	768	−0.09	3.52	768	−0.30	8.31
SON	21	−5.30	11.63	21	3.72	4.22	21	1.75	4.43
SPA	144	−3.83	17.21	144	−6.21	16.89	144	−6.17	43.61
SPG	24	1.27	6.45	24	−1.16	3.21	24	−3.49	5.32
SPT	512	0.53	9.40	512	−0.07	3.52	512	0.77	5.20
SRE	86	−0.44	8.55	86	0.30	6.14	86	−13.90	53.19
SSH	564	0.34	14.58	564	0.38	3.03	564	0.90	6.49
SSO	213	−0.74	13.70	213	0.02	4.37	213	−1.43	10.95
STJ	592	−1.06	8.94	592	0.13	6.29	592	0.25	7.71
STO	17	1.83	3.41	17	−0.35	6.77	17	−0.70	4.95
STT	30	−0.93	3.16	30	−1.73	1.37	30	−1.14	1.66
SUA	755	−0.31	11.57	755	0.73	8.70	755	0.31	10.52
SVD	229	0.56	21.73	229	−1.21	7.91	229	0.04	6.66
SWI	27	−1.26	6.00	27	−0.39	1.85	27	0.81	15.40
SYO	25	−9.49	35.10	25	5.79	23.43	25	2.32	38.73
TAH	3	11.70	18.69	3	−16.94	26.54	3	4.35	5.71
TAM	374	1.95	11.31	374	−1.08	6.20	374	−3.71	5.58
TAN	291	4.65	15.61	291	1.59	10.55	291	0.31	9.75
TCN	6	7.69	23.87	6	−1.35	16.33	6	10.65	17.56
TDC	112	−1.36	7.37	112	−0.69	1.98	112	0.87	2.53
TEH	49	−4.61	31.61	49	−1.71	52.24	49	−9.75	79.93
TEN	299	1.61	19.13	299	0.41	8.20	299	0.52	15.86
TEO	463	4.78	38.05	463	−0.12	29.40	463	1.37	46.72
TFS	531	0.61	13.13	531	−0.14	5.46	531	−0.72	8.15

Table 2 (continued)

Observatory code	N_x	m_x	σ_x	N_y	m_y	σ_y	N_z	m_z	σ_z
THJ	214	0.69	11.19	214	0.42	2.32	214	0.28	2.40
THL	792	−0.14	4.87	792	−0.57	3.68	792	0.16	16.56
THY	792	−0.20	9.66	792	0.78	6.68	792	−0.05	8.38
TIK	246	1.49	13.89	246	0.55	6.83	246	−0.60	21.57
TIR	163	−0.14	13.05	163	1.40	7.07	163	1.40	5.37
TKH	8	1.21	6.81	8	−0.34	3.98	8	−38.83	12.69
TKT	344	2.14	13.77	344	−0.74	5.04	344	−0.10	6.32
TMK	11	0.70	6.10	11	−3.49	6.24	11	1.62	27.00
TNB	13	1.30	11.24	13	−0.87	16.47	13	−0.81	13.29
TND	78	−1.87	18.02	78	0.14	8.18	78	−2.30	9.05
TNG	71	0.52	32.99	71	−0.16	20.74	71	15.25	76.80
TOL	81	0.48	12.84	81	−0.17	3.97	81	1.65	7.08
TOO	109	−0.09	8.96	109	0.07	3.51	109	0.19	6.23
TRD2	14	5.48	7.84	14	1.32	10.97	14	2.59	12.77
TRO	405	−2.27	14.75	405	0.25	4.25	405	−0.16	11.95
TRW	709	0.89	19.86	709	−0.73	14.41	709	−0.44	9.26
TSU	620	−0.31	13.11	620	3.17	5.69	620	0.17	4.06
TTB2	211	−3.35	14.12	211	0.01	11.53	211	0.64	9.44
TUC1	432	1.08	12.30	432	0.43	3.65	432	−0.15	5.31
TUC2	352	0.65	8.12	352	0.15	12.75	352	−1.20	10.88
TUL	5	−0.06	76.23	5	−5.07	155.32	5	−0.22	161.43
TUN	18	2.33	13.15	18	−7.33	20.94	18	−4.01	21.25
UBA	21	−5.58	11.33	21	−0.03	4.17	21	2.44	6.18
UJJ	266	0.19	15.95	266	−2.55	13.15	266	−0.27	9.18
UPS	233	1.13	4.84	233	−0.12	2.31	233	−1.16	4.55
VAL	744	0.06	6.96	744	0.27	3.31	744	−0.18	6.24
VIC	730	−0.30	8.15	730	0.42	3.99	730	0.16	6.55
VLA	352	1.48	16.32	352	4.08	10.58	352	0.80	10.44
VNA2	137	−0.59	13.18	137	−6.66	18.25	137	0.30	7.48
VNA3	96	0.09	5.30	96	−1.45	5.58	96	0.31	4.14
VOS	511	2.76	23.99	511	−0.84	34.22	511	0.50	31.20
VSK	198	1.92	15.31	198	−2.63	10.91	198	−1.40	25.63
VSS	457	2.20	24.06	457	−1.34	14.28	457	1.00	16.70
WAT	24	0.10	12.49	24	0.61	1.77	24	−5.67	13.15
WHN	579	1.25	13.87	579	−0.07	3.83	579	0.12	5.70
WHS	2	1.39	11.67	2	1.38	1.88	2	7.39	14.38
WIC	84	0.45	4.88	84	0.16	2.01	84	0.05	3.23
WIK	639	−0.43	8.58	639	0.19	3.31	639	−0.46	6.01
WIL	13	12.28	10.92	13	−0.43	5.96	13	9.40	15.82
WIT	361	0.37	6.83	361	0.02	3.01	361	−0.12	5.67
WMQ	20	1.20	7.51	20	0.31	2.52	20	−0.90	4.53
WNG	778	0.00	6.56	778	−0.01	2.74	778	−0.25	6.02
YAK	559	0.19	10.10	559	−0.32	4.58	559	−0.43	12.16
YKC2	489	0.48	12.65	489	−0.06	8.45	489	−0.93	15.61
YSS	374	4.25	12.66	374	1.89	9.23	374	−0.69	7.40
ZUY	2	0.11	0.39	2	0.60	0.09	2	0.11	1.17

Acknowledgements

The authors would like to express their gratitude to scientists working at magnetic observatories, data suppliers and involved national institutes for making geomagnetic observatory data available, to the World Data Centre for Geomagnetism (Edinburgh) for compiling these data in a database. We thank two anonymous reviewers for the valuable comments. Figures are made using the free software GMT (Wessel et al. 2013) and *gnuplot*. The publication costs were paid from the French Agence Nationale der Recherche, project DYRE-COMB (grant ANR-22-CE49-0016-01).

Author Contributions

I. Wardinski organized the manuscript based on the analyses of the contributing co-authors. All authors contributed modeling results and/or detailed technical analyses and/or discussions for this study. All co-authors have read and approved the manuscript.

Funding

Not applicable.

Data Availability

The datasets used and/or analyzed during the current study are available from the corresponding author on reasonable request.

Declarations

Conflict of interest

The authors declare that they have no conflict of interest.

Author details

[1]Institut Terre et Environnement Strasbourg, Ecole et Observatoire des Sciences de La Terre, Université de Strasbourg, CNRS, UMR7063, Strasbourg, France. [2]Laboratoire de Planétologie et Géosciences, Nantes Université, Univ Angers, Le Mans Université, CNRS UMR 6112, 2 rue de la Houssiniére, 44000 Nantes, France. [3]Present Address: Université Paris Cité, Institut de physique du globe de Paris, CNRS, 75005 Paris, France.

Received: 1 October 2025 Accepted: 28 February 2026

References

Abramowitz M, Stegun IA (1973) Handbook of Mathematical Functions. Dover (New York)

Alken P, Thébault E, Beggan CD, Amit H, Aubert J, Baerenzung J, Bondar TN, Brown WJ, Califf S, Chambodut A, Chulliat A, Cox GA, Finlay CC, Fournier A, Gillet N, Grayver A, Hammer MD, Holschneider M, Huder L, Hulot G, Jager T, Kloss C, Korte M, Kuang W, Kuvshinov A, Langlais B, Léger JM, Lesur V, Livermore PW, Lowes FJ, Macmillan S, Magnes W, Mandea M, Marsal S, Matzka J, Metman MC, Minami T, Morschhauser A, Mound JE, Nair M, Nakano S, Olsen N, Pavón-Carrasco FJ, Petrov VG, Ropp G, Rother M, Sabaka TJ, Sanchez S, Saturnino D, Schnepf NR, Shen X, Stolle C, Tangborn A, Tøffner-Clausen L, Toh H, Torta JM, Varner J, Vervelidou F, Vigneron P, Wardinski I, Wicht J, Woods A, Yang Y, Zeren Z, Zhou B (2021) International geomagnetic reference field: the thirteenth generation. Earth Planets Space 73(1):49

Alken P, Thébault E, Beggan CD, Aubert J, Baerenzung J, Brown WJ, Califf S, Chulliat A, Cox GA, Finlay CC, Fournier A, Gillet N, Hammer MD, Holschneider M, Hulot G, Korte M, Lesur V, Livermore PW, Lowes FJ, Macmillan S, Nair M, Olsen N, Ropp G, Rother M, Schnepf NR, Stolle C, Toh H, Vervelidou F, Vigneron P, Wardinski I (2021) Evaluation of candidate models for the 13th generation International Geomagnetic Reference Field. Earth Planets Space 73(1):48

Amit H (2014) Can downwelling at the top of the Earth's core be detected in the geomagnetic secular variation? Phys Earth Planet Inter 229:110–121

Arkani-Hamed J, Zhao SK, Strangway DW (1988) Geophysical interpretation of the magnetic anomalies of China derived from Magsat data. Geophys J Int 95:347–359

Aubert J, Amit H, Hulot G, Olson P (2008) Thermochemical flows couple the Earth's inner core growth to mantle heterogeneity. Nature 454(7205):758–761

Backus GE (1983) Application of mantle filter theory to the magnetic jerk of 1969. Geophys J Roy Astron Soc 74(3):713–746

Benton ER, Whaler KA (1983) Rapid diffusion of the poloidal geomagnetic field through the weakly conducting mantle: a perturbation solution. Geophys J 75(1):77–100

British Geological Survey - Edinburgh (2020) Worldwide observatory annual means. http://www.geomag.bgs.ac.uk/data_service/data/annual_means.shtml

Broomhead DS, King GP (1986) Extracting qualitative dynamics from experimental data. Physica D 20:217–236

Brown WJ, Mound JE, Livermore PW (2013) Jerks abound: an analysis of geomagnetic observatory data from 1957 to 2008. Phys Earth Planet Inter 223:62–76

Cain JC, Wang Z, Kluth C, Schmitz DR (1989) Derivation of a geomagnetic model to $n = 63$. Geophys J R astr Soc 97:431–441

Christensen U, Olson P, Glatzmaier GA (1998) A dynamo model interpretation of geomagnetic field structures. Geophys Res Lett 25(10):1565–1568

Colas M, Terra-Nova F, Amit H (2025) The history of geomagnetic secular variation hemispherical dichotomies. Phys Earth Planet Inter 363:107352

Constable C, Johnson C (2005) A paleomagnetic power spectrum. Phys Earth Planet Inter 153:61–73

de Oliveira WP, Hartmann GA, Terra-Nova F, Pasqualon NG, Savian JF, Lima EF, da Luz FR, Trindade RIF (2024) Long-term persistency of a strong non-dipole field in the South Atlantic. Nat Commun 15(1):9447

Dumberry M, Finlay CC (2007) Eastward and westward drift of the Earth's magnetic field for the last three millennia. Earth Planet Sci Lett 254:146–157

Finlay CC, Jackson A (2003) Equatorially dominated magnetic field change at the surface of Earth's core. Science 300:2084–2086

Finlay CC, Maus S, Beggan CD, Bondar TN, Chambodut A, Chernova TA, Chulliat A, Golovkov VP, Hamilton B, Hamoudi M, Holme R, Hulot G, Kuang W, Langlais B, Lesur V, Lowes FJ, Lühr H, MacMillan S, Mandea M, McLean S, Manoj C, Menvielle M, Michaelis I, Olsen N, Rauberg J, Rother M, Sabaka TJ, Tangborn A, Tøffner-Clausen L, Thébault E, Thomson AWP, Wardinski I, Wei Z, Zvereva TI (2010) International Geomagnetic Reference Field: the eleventh generation. Geophys J Int 183:1216–1230

Finlay CC, Olsen N, Kotsiaros S, Gillet N, Tøffner-Clausen L (2016) Recent geomagnetic secular variation from Swarm and ground observatories as estimated in the CHAOS-6 geomagnetic field model. Earth Planets Space 68(1):112

Finlay CC, Kloss C, Olsen N, Hammer MD, Tøffner-Clausen L, Grayver A, Kuvshinov A (2020) The CHAOS-7 geomagnetic field model and observed changes in the South Atlantic Anomaly. Earth Planets Space 72(1):156

Ghil M, Allen MR, Dettinger MD, Ide K, Kondrashov D, Mann ME, Robertson AW, Saunders A, Tian Y, Varadi F, Yiou P (2002) Advanced spectral methods for climatic time series. Rev Geophys 40:1–41

Golyandina N, Nekrutkin V, Zhigljavsky A (2001) Analysis of Time Series Structure: SSA and Related Techniques. Chapman & Hall

Hammer MD, Finlay CC (2019) Local averages of the core-mantle boundary magnetic field from satellite observations. Geophys J Int 216(3):1901–1918

Holme R (1998) Electromagnetic Core-Mantle Coupling II: Probing Deep Mantle Conductance. American Geophysical Union (AGU), pp. 139–151

Holme R, Olsen N, Bairstow FL (2011) Mapping geomagnetic secular variation at the core-mantle boundary. Geophys J Int 186(2):521–528

Holme R, Olsen N, Rother M, Lühr H (2003) CO2, A Champ Magnetic Field Model. Springer, Berlin Heidelberg, pp 220–225

Hulot G, Eymin C, Langlais B, Mandea M, Olsen N (2002) Small-scale structure of the geodynamo inferred from Oersted and Magsat satellite data. Nature 416(6881):620–623

Hulot G, Lhuillier F, Aubert J (2010) Earth's dynamo limit of predictability. Geophys Res Lett 37:6305

INTERMAGNET (2020) INTERMAGNET - the global network of observatories, monitoring the Earth's magnetic field. http://intermagnet.org

Jackson A, Jonkers ART, Walker MR (2000) Four centuries of geomagnetic secular variation from historical records. Philos Trans R Soc London, Ser A 358:957–990

Lesur V, Wardinski I, Rother M, Mandea M (2008) GRIMM: the GFZ Reference Internal Magnetic Model based on vector satellite and observatory data. Geophys J Int 173(2):382–394

Lesur V, Wardinski I, Asari S, Minchev B, Mandea M (2010) Modelling the Earth's core magnetic field under flow constraints. Earth Planets Space 62:503–516

Lesur V, Wardinski I, Hamoudi M, Rother M (2010) The second generation of the GFZ Reference Internal Magnetic Model: GRIMM-2. Earth Planets Space 62(10):765–773

Lesur V, Rother M, Wardinski I, Schachtschneider R, Hamoudi M, Chambodut A (2015) Parent magnetic field models for the IGRF-12GFZ-candidates. Earth Planets Space 67:87

Lesur V, Wardinski I, Baerenzung J, Holschneider M (2018) On the frequency spectra of the core magnetic field Gauss coefficients. Phys Earth Planet Inter 276:145–158

Lesur V, Gillet N, Hammer MD, Mandea M (2022) Rapid variations of earth's core magnetic field. Surv Geophys 43(1):41–69

Lézin M, Amit H, Terra-Nova F, Wardinski I (2023) Mantle-driven north-south dichotomy in geomagnetic polar minima. Phys Earth Planet Inter 337:107000

Livermore PW, Hollerbach R, Finlay CC (2017) An accelerating high-latitude jet in Earth's core. Nat Geosci 10(1):62–68

Lowes FJ (1966) Mean-square values on sphere of spherical harmonic vector fields. J Geophys Res 71:2179

Mauersberger P (1956) Das Mittel der Energiedichte des geomagnetischen Hauptfeldes an der Erdoberfläche und seine säkulare Änderung. Gerlands Beitr Geophys 65:207–215

Mound JE, Davies CJ (2023) Longitudinal structure of Earth's magnetic field controlled by lower mantle heat flow. Nat Geosci 16(4):380–385

Olsen N, Lühr H, Sabaka TJ, Mandea M, Rother M, Tøffner-Clausen L, Choi S (2006) CHAOS-a model of the Earth's magnetic field derived from CHAMP, Ørsted, and SAC-C magnetic satellite data. Geophys J Int 166(1):67–75

Pavón-Carrasco FJ, Marsal S, Campuzano SA, Torta JM (2021) Signs of a new geomagnetic jerk between 2019 and 2020 from Swarm and observatory data. Earth Planets Space 73(1):175

Plaut G, Vautard R (1994) Spells of low-frequency oscillations and weather regimes in the northern hemisphere. J Atmos Sci 51:210–236

Ropp G, Lesur V, Baerenzung J, Holschneider M (2020) Sequential modelling of the Earth's core magnetic field. Earth Planets Space 72(1):153

Terra-Nova F, Wardinski I (2023) Regional outer core kinematics from the time dependence of intense geomagnetic flux patches. Phys Earth Planet Inter 344:107106

Terra-Nova F, Amit H, Hartmann GA, Trindade RIF, Pinheiro KJ (2017) Relating the South Atlantic Anomaly and geomagnetic flux patches. Phys Earth Planet Inter 266:39–53

Thébault E, Finlay CC, Beggan CD, Alken P, Aubert J, Barrois O, Bertrand F, Bondar T, Boness A, Brocco L, Canet E, Chambodut A, Chulliat A, Coïsson P, Civet F, Du A, Fournier A, Fratter I, Gillet N, Hamilton B, Hamoudi M, Hulot G, Jager T, Korte M, Kuang W, Lalanne X, Langlais B, Léger J-M, Lesur V, Lowes FJ, Macmillan S, Mandea M, Manoj C, Maus S, Olsen N, Petrov V, Ridley V, Rother M, Sabaka TJ, Saturnino D, Schachtschneider R, Sirol O, Tangborn A, Thomson A, Tøffner-Clausen L, Vigneron P, Wardinski I, Zvereva T (2015) International Geomagnetic Reference Field: the 12th generation. Earth Planets Space 67:79

Toksöz MN, Arkani-Hamed J, Knight CA (1969) Geophysical data and long-wave heterogeneities of the Earth's mantle. J Geophys Res 74:3751–3770

Torta JM, Pavón-Carrasco FJ, Marsal S, Finlay CC (2015) Evidence for a new geomagnetic jerk in 2014. Geophys Res Lett 42(19):7933–7940

Vautard R, Yiou P, Ghil M (1992) Singular-spectrum analysis: a toolkit for short, noisy chaotic signals. Physica D 58:95–126

Wardinski I, Holme R (2006) A time-dependent model of the Earth's magnetic field and its secular variation for the period 1980 to 2000. J Geophys Res (Solid Earth) 111:12101

Wardinski I, Holme R (2011) Signal from noise in geomagnetic field modelling: denoising data for secular variation studies. Geophys J Int 185:653–662

Wardinski I, Lesur V (2012) An extended version of the C^{3}FM geomagnetic field model: application of a continuous frozen-flux constraint. Geophys J Int 189:1409–1429

Wardinski I, Saturnino D, Amit H, Chambodut A, Langlais B, Mandea M, Thébault E (2020) Geomagnetic core field models and secular variation forecasts for the 13th International Geomagnetic Reference Field (IGRF-13). Earth Planets Space 72(1):155

Wardinski I, Amit H, Langlais B, Thébault E (2021) The internal structure of mercury's core inferred from magnetic observations. J Geophys Res 126(12):e06792

Wardinski I, Terra-Nova F, Thébault E (2025) Evaluation of archeo- and paleomagnetic field models and their common features. Phys Earth Planet Inter 366:107399

Wessel P, Smith WHF, Scharroo R, Luis J, Wobbe F (2013) Generic mapping tools: improved version released. EOS Trans 94(45):409–410

Whaler KA, Hammer MD, Finlay CC, Olsen N (2022) Core surface flow changes associated with the 2017 Pacific Geomagnetic Jerk. Geophys Res Lett 49(15):e98616

World Data Centre for Geomagnetism - Edinburgh (2019) Geomagnetic Data Master Catalogue. http://www.wdc.bgs.ac.uk/catalog/master.html

Publisher's Note